General mechanisms for stabilizing weakly compressible models

Jinhua Lu[1,*] and Nikolaus A. Adams[1,2]
[1]*Department of Mechanical Engineering, Chair of Aerodynamics and Fluid Mechanics, Technical University of Munich, Boltzmannstraße 15, Garching 85748, Germany*
[2]*Munich Institute of Integrated Materials, Energy and Process Engineering, Technical University of Munich, Lichtenbergstraße 4a, Garching 85748, Germany*

(Received 24 November 2022; accepted 26 April 2023; published 17 May 2023)

Many weakly compressible models with intrinsic mechanisms for stabilizing computation have been proposed to simulate incompressible flows. The present paper analyzes several weakly compressible models to establish general mechanisms that incorporate them into a unified and simple framework. It is found that all these models contain some identical numerical dissipation terms, mass diffusion terms in the continuity equation, and bulk viscosity terms in the momentum equation. They are proven to provide general mechanisms for stabilizing computation. Referring to the general mechanisms and the computational procedures of the lattice Boltzmann flux solver, two general weakly compressible solvers for isothermal flows and thermal flows are proposed. They can be directly derived from standard governing equations and implicitly introduce those numerical dissipation terms. Detailed numerical investigations demonstrate that the two general weakly compressible solvers have good numerical stability and accuracy for both isothermal and thermal flows, which validates the general mechanisms further and the general approach of constructing general weakly compressible solvers.

DOI: 10.1103/PhysRevE.107.055306

I. INTRODUCTION

Incompressible flow is a common phenomenon in both natural and engineering applications. According to the ways to update pressure, the numerical algorithms for simulations of incompressible flows can be classified into two categories. The first category is the exactly incompressible model whose governing equations are

$$\partial_\alpha u_\alpha = 0, \tag{1}$$

$$\partial_t(\rho_0 u_\alpha) + \partial_\beta(\rho_0 u_\alpha u_\beta) = -\partial_\alpha p + \mu\partial_\beta(\partial_\alpha u_\beta + \partial_\beta u_\alpha), \tag{2}$$

where u_α is the velocity, ρ_0 is the constant fluid density, p is the pressure, and μ is the dynamic viscosity. It can be seen from the governing equations that the velocity can be updated explicitly, while the pressure needs to be updated implicitly. The well-known algorithms include the semi-implicit method for the pressure-linked equation (SIMPLE) [1], SIMPLE revised [2], SIMPLE consistent [3], pressure implicit with split operator (PISO) [4], and so on. On the one hand, these algorithms require complicated iteration steps to update pressure due to the implicit pressure equation. On the other hand, without the pressure wave induced by compressibility, these algorithms, in general, have good numerical stability.

The second category is the weakly compressible model, where the pressure is updated explicitly. The earliest weakly compressible model is the artificial compressibility method (ACM) [5]. The governing equations are

$$\partial_t\rho + \partial_\alpha(\rho_0 u_\alpha) = 0,\ p = \rho c_s^2, \tag{3}$$

$$\partial_t(\rho_0 u_\alpha) + \partial_\beta(\rho_0 u_\alpha u_\beta) = -\partial_\alpha p + \mu\partial_\beta(\partial_\alpha u_\beta + \partial_\beta u_\alpha), \tag{4}$$

where ρ_0 is the constant fluid density, ρ is the reference density related to pressure, and c_s is the sound speed. Here, the pressure equation [Eq. (3)] neglects the higher-order term $\partial_\alpha(\delta\rho u_\alpha)$ compared with the standard continuity equation $\partial_t\rho + \partial_\alpha(\rho u_\alpha) = 0$, where $\delta\rho$ is the density perturbation defined by $\rho = \rho_0 + \delta\rho$. Consequently, the pressure is decoupled from fluid density. Due to the pressure wave's existence, directly solving the governing equations with central difference schemes suffers from numerical instability. Additional treatments, such as specified discretization schemes [6] and numerical dissipation terms [7,8], are needed to stabilize computation.

The linkwise artificial compressibility method (LWACM) [9] uses the lattice framework of the lattice Boltzmann method (LBM) [10] to solve the weakly compressible Navier-Stokes equations. It belongs to the community of artificial compressibility methods as well.

The second weakly compressible model is the LBM [10], a mesoscopic method based on the Boltzmann equation. Using the Chapman-Enskog expansion analysis, the following standard governing equations can be approximately recovered with second-order accuracy.

$$\partial_t\rho + \partial_\alpha(\rho u_\alpha) = 0, \tag{5}$$

$$\partial_t(\rho u_\alpha) + \partial_\beta(\rho u_\alpha u_\beta) = -\partial_\alpha p + \mu\partial_\beta(\partial_\alpha u_\beta + \partial_\beta u_\alpha). \tag{6}$$

Based on the original LBM [10], some improved models have been developed to overcome its intrinsic drawbacks, including the dependence on uniform meshes, coupled time step with mesh size, and extra memory size. By combing the lattice Boltzmann equation (LBE) with a fixed relaxation

---

[*] Corresponding author: jinhua.lu@tum.de

time $\tau = 1$ and a corrector step to recover the correct viscous forcing term, a fractional step LBM (FSLBM) [11] was proposed to decrease the memory size. It was found to have good numerical stability at high Reynolds number flows, even for the inviscid flow. By adopting a second-order approximation for LBE, the simplified LBM (SLBM) [12–15] was also proposed to decrease the memory size. It has been proven to have good numerical stability for high Reynolds number flows [15]. Besides, the lattice Boltzmann flux solver (LBFS) [16,17] was proposed to overcome the three drawbacks of the LBM. Based on the finite-volume scheme, it constructs a simplified LBE at the cell face to calculate fluxes. It can simulate both viscous and inviscid flows.

The LBM and related models can recover the two kinds of governing equations mentioned above, Eqs. (3)–(6), approximately. Therefore, they are intrinsically weakly compressible models. From a macroscopic perspective, these models should have additional treatments to stabilize computation. According to recent research [18–20], the mechanisms of stabilizing computation in these models can be identified as different numerical dissipation terms. Therefore, a fundamental problem is whether general numerical dissipation terms exist for stabilizing weakly compressible models. If such general terms can be found, many weakly compressible models can be incorporated into a unified, simple framework. This objective motivates the present work.

The present paper analyzes several weakly compressible models [9–11,15,20,21]. It is found that these models contain some identical numerical dissipation terms, which provide general mechanisms for stabilizing computations. Based on such general mechanisms and referring to computational procedures of LBFS, a general approach, which introduces numerical dissipation terms implicitly, is proposed to construct general weakly compressible solvers from governing equations. The general weakly compressible solver for isothermal flow (GWCSIF) is proposed first. Numerical investigations demonstrate that GWCSIF has good numerical stability for high Reynolds number flows. It is validated by simulating viscous and inviscid, transient and steady, and two-dimensional (2D) and three-dimensional (3D) incompressible flows. Based on the general approach, a general weakly compressible solver for thermal flow (GWCSTF) is also proposed. Numerical investigations also demonstrate that GWCSTF has good numerical stability for high Rayleigh number flows.

The remaining parts of the paper are organized as follows: weakly compressible models are analyzed in Sec. II, and general mechanisms for stabilizing computation are identified; GWCSIF is constructed and analyzed in Sec. III, and it is validated by numerical tests in Sec. IV; GWCSTF is constructed in Sec. V and validated by numerical tests in Sec. VI; conclusions are given in Sec. VII.

II. ANALYSES OF WEAKLY COMPRESSIBLE MODELS

It has been proven that the mechanisms for stabilizing computation in some weakly compressible models [18–20] can be explained by numerical dissipation terms. The present section analyzes several weakly compressible models to identify general numerical dissipation terms for stabilizing computations.

A. Analysis of LBM

To illustrate the derivations of the macroscopic equations of weakly compressible models based on LBM, LBM is introduced here.

1. LBM

The evolution equation of LBM [10] is

$$f_i(\mathbf{x} + \mathbf{e}_i\delta t, t + \delta t) = f_i(\mathbf{x}, t) - \frac{1}{\tau}\big[f_i(\mathbf{x}, t) - f_i^{\mathrm{eq}}(\mathbf{x}, t)\big], \quad (7)$$

$$f_i^{\mathrm{eq}} = w_i\rho\left[1 + \frac{e_{i\alpha}u_\alpha}{c_s^2} + \frac{(e_{i\alpha}u_\alpha)^2}{2c_s^4} - \frac{u_\alpha u_\alpha}{2c_s^2}\right], \quad (8)$$

where $\mathbf{e}_i$ is the discrete velocity; f_i and f_i^{eq} are distribution function and equilibrium distribution function in discrete velocity $\mathbf{e}_i$, respectively; τ is the relaxation parameter, δt is the time interval; w_i is the weight coefficient. The discrete velocities and weight coefficients of different models can be seen in Ref. [10]. The equilibrium distribution functions satisfy

$$\sum_i f_i^{\mathrm{eq}} = \rho, \quad \sum_i f_i^{\mathrm{eq}} e_{i\alpha} = \rho u_\alpha,$$
$$\sum_i f_i^{\mathrm{eq}} e_{i\alpha}e_{i\beta} = \rho c_s^2\delta_{\alpha\beta} + \rho u_\alpha u_\beta,$$
$$\sum_i f_i^{\mathrm{eq}} e_{i\alpha}e_{i\beta}e_{i\gamma} = \rho c_s^2(u_\alpha\delta_{\beta\gamma} + u_\beta\delta_{\alpha\gamma} + u_\gamma\delta_{\alpha\beta}), \quad (9)$$

where subscripts α and β denote coordinate components. The macroscopic pressure, velocity, and kinematic viscosity are determined by

$$\rho = \sum_i f_i, \quad p = \rho c_s^2, \quad (10)$$

$$\rho u_\alpha = \sum_i f_i e_{i\alpha}, \quad (11)$$

$$\upsilon = \mu/\rho = (\tau - 0.5)c_s^2\delta t. \quad (12)$$

2. Macroscopic equations recovered from LBE

It has been proven that by using the Chapman-Enskog expansion analysis, LBE can recover the continuous governing equations, Eqs. (5) and (6), with second-order accuracy [10]. However, LBM is a discrete algorithm. To explain its mechanisms for stabilizing computation, the discretized rather than continuous governing equations need to be recovered. Therefore, the more actual macroscopic equations (MAMEs) [18] with actual numerical dissipation terms are derived to explain the good numerical stability of LBM. The derived MAMEs are

$$\rho^{n+1} = \rho^n - \partial_\alpha(\rho u_\alpha)^n\delta t + 0.5\delta t^2\partial_\alpha\partial_\beta(\rho u_\alpha u_\beta + \rho c_s^2\delta_{\alpha\beta})^n + O(\delta t^3), \quad (13)$$

$$\begin{aligned}(\rho u_\alpha)^{n+1} = {} & (\rho u_\alpha)^n - \partial_\beta(\rho u_\alpha u_\beta + \rho c_s^2\delta_{\alpha\beta})^n\delta t \\ & + \upsilon\delta t\partial_\beta[\partial_\beta(\rho u_\alpha) + \partial_\alpha(\rho u_\beta) + \partial_\gamma(\rho u_\gamma)\delta_{\alpha\beta}]^n \\ & + \big(\upsilon/c_s^2 - 0.5\delta t\big)\delta t\partial_t\partial_\beta\big(\rho u_\alpha u_\beta + \rho c_s^2\delta_{\alpha\beta}\big)^n \\ & + O(\delta t^3). \end{aligned} \quad (14)$$

Subsequent research indicates that some additional terms in MAMEs are unnecessary, and simplified MAMEs [21] have been proposed. The equations are

$$\rho^{n+1} = \rho^n - \partial_\alpha(\rho u_\alpha)^n\delta t + 0.5\delta t^2\partial_\alpha\partial_\beta\left(\rho c_s^2\delta_{\alpha\beta}\right)^n, \tag{15}$$

$$\begin{aligned}(\rho u_\alpha)^{n+1} = {}& (\rho u_\alpha)^n - \partial_\beta\left(\rho u_\alpha u_\beta + \rho c_s^2\delta_{\alpha\beta}\right)^n\delta t \\ & + \upsilon\delta t\partial_\beta\partial_\beta(\rho u_\alpha)^n - \left(\upsilon + 0.5c_s^2\delta t\right) \\ & \times[\partial_\alpha\rho^{n+1} - \partial_\alpha\rho^n].\end{aligned} \tag{16}$$

Both additional terms in the density and momentum equations help stabilize computations [21].

Substituting Eq. (15) into Eq. (16), the momentum equation can be rewritten as

$$\begin{aligned}(\rho u_\alpha)^{n+1} = {}& (\rho u_\alpha)^n - \partial_\beta\left(\rho u_\alpha u_\beta + \rho c_s^2\delta_{\alpha\beta}\right)^n\delta t \\ & + \upsilon\delta t\partial_\beta\partial_\beta(\rho u_\alpha)^n + \left(\upsilon + 0.5c_s^2\delta t\right) \\ & \times\left[\partial_\alpha\partial_\beta\left(\rho u_\beta\right)^n - 0.5c_s^2\delta t\partial_\alpha\partial_\beta\partial_\gamma\left(\rho c_s^2\delta_{\beta\gamma}\right)^n\right].\end{aligned} \tag{17}$$

It can be seen that the additional terms contain a mass diffusion term related to $\partial_\alpha\partial_\beta(\rho\delta_{\alpha\beta})^n$ in the continuity equation and a bulk viscosity term related to $\partial_\alpha(\partial_\beta u_\beta)^n$ in the momentum equation.

B. Analysis of SLBM

SLBM is a second-order approximation of LBM. The early SLBM [12] has obvious numerical diffusion affecting the accuracy. Later, the improved model [15] was proposed. The present analysis is based on the improved model [15]. The procedures of the model are listed as follows:

Predictor step:

$$\rho^* = \sum_i f_i^{\text{eq}}(\mathbf{x} - \mathbf{e}_i\delta t, t), \tag{18}$$

$$\rho^* u_\alpha^* = \sum_i f_i^{\text{eq}}(\mathbf{x} - \mathbf{e}_i\delta t, t)e_{i\alpha}. \tag{19}$$

Corrector step:

$$\rho^{n+1} = \rho^*, \tag{20}$$

$$\begin{aligned}(\rho u_\alpha)^{n+1} = {}& \rho^* u_\alpha^* + (\tau - 1)\sum_i e_{i\alpha} f_i^{\text{eq}}(\mathbf{x} + \mathbf{e}_i\delta t, t + \delta t) \\ & - (\tau - 1)\rho^n u_\alpha^n,\end{aligned} \tag{21}$$

where the subscript * represents the predicted variables.

By using a Taylor series expansion, the second-order macroscopic equations [19] are given as follows:

Predictor step:

$$\rho^* = \rho^n - \partial_\alpha(\rho u_\alpha)^n\delta t + 0.5\delta t^2\partial_\alpha\partial_\beta\left(\rho u_\alpha u_\beta + \rho c_s^2\delta_{\alpha\beta}\right)^n, \tag{22}$$

$$\begin{aligned}(\rho u_\alpha)^* = {}& -\partial_\beta\left(\rho u_\alpha u_\beta + \rho c_s^2\delta_{\alpha\beta}\right)^n\delta t + 0.5c_s^2\delta t^2\partial_\beta \\ & \times[\partial_\beta(\rho u_\alpha) + 2\partial_\gamma(\rho u_\gamma)\delta_{\alpha\beta}]^n.\end{aligned} \tag{23}$$

Corrector step:

$$\rho^{n+1} = \rho^*, \tag{24}$$

$$(\rho u_\alpha)^{n+1} = \rho^* u_\alpha^* + (\tau - 1)\begin{Bmatrix}\rho u_\alpha + \delta t\partial_\beta\left(\rho u_\alpha u_\beta + \rho c_s^2\delta_{\alpha\beta}\right) \\ +0.5c_s^2\delta t^2\partial_\beta[\partial_\beta(\rho u_\alpha) + \partial_\alpha(\rho u_\beta) + \partial_\gamma(\rho u_\gamma)\delta_{\alpha\beta}]\end{Bmatrix}^* - (\tau - 1)\rho u_\alpha. \tag{25}$$

It can be seen that there is a mass diffusion term in the continuity equation. The momentum equation can be rewritten as

$$\begin{aligned}(\rho u_\alpha)^{n+1} = {}& (\rho u_\alpha)^n - \delta t\partial_\beta\left(\rho c_s^2\delta_{\alpha\beta}\right)^n + \tau\left\{-\delta t\partial_\beta(\rho u_\alpha u_\beta) + \tfrac{1}{2}c_s^2\delta t^2[\partial_\beta\partial_\beta(\rho u_\alpha) + 2\partial_\alpha\partial_\beta(\rho u_\beta)]\right\}^n \\ & + (\tau - 1)\left\{\delta t\partial_\beta(\rho u_\alpha u_\beta) + \tfrac{1}{2}c_s^2\delta t^2[\partial_\beta\partial_\beta(\rho u_\alpha) + 2\partial_\alpha\partial_\beta(\rho u_\beta)]\right\}^* \\ & + (\tau - 1)c_s^2\delta t\partial_\alpha\left[-\partial_\beta(\rho u_\beta)^n\delta t + 0.5\delta t^2\partial_\beta\partial_\gamma\left(\rho u_\beta u_\gamma + \rho c_s^2\delta_{\beta\gamma}\right)^n\right].\end{aligned} \tag{26}$$

It can be seen that it contains bulk viscosity terms in $\tau\rho^n c_s^2\delta t^2\partial_\alpha(\partial_\beta u_\beta)^n$, $(\tau-1)\rho^* c_s^2\delta t^2\partial_\alpha(\partial_\beta u_\beta)^*$, and $-(\tau-1)\rho^n c_s^2\delta t^2(\partial_\alpha u_\alpha)^n$.

C. Analysis of FSLBM

The original FSLBM [11] is based on the standard LBM [10]. Later, FSLBM based on the incompressible LBM [22] was proposed to decouple the fluid density and pressure. The present analysis is for the FSLBM based on the incompressible LBM [23].

The model consists of two steps:

Predictor step:

$$f_i(\mathbf{x}, t + \delta t) = f_i^{\text{eq}}(\mathbf{x} - \mathbf{e}_i\delta t, t), \tag{27}$$

where $f_i^{\text{eq}} = w_i\rho + w_i\rho_0[\frac{e_{i\alpha}u_\alpha}{c_s^2} + \frac{(e_{i\alpha}u_\alpha)^2}{2c_s^4} - \frac{u_\alpha u_\alpha}{2c_s^2}]$. The predicted pressure and velocity are

$$\rho^* = \sum_i f_i, \quad p = \rho c_s^2, \tag{28}$$

$$\rho_0 u_\alpha^* = \sum_i f_i e_{i\alpha}. \tag{29}$$

Corrector step:

$$\rho^{n+1} = \rho^*, \tag{30}$$

$$u_\alpha^{n+1} = u_\alpha^* + \left(\upsilon - 0.5c_s^2\delta t\right)\delta t\partial_\beta\partial_\beta u_\alpha. \tag{31}$$

By using a second-order Taylor series expansion, $f_i^{\mathrm{eq}}(\mathbf{x}-\mathbf{e}_i\delta t,t)$ is expanded as

$$
\begin{aligned}
f_i^{\mathrm{eq}}&(\mathbf{x}-\mathbf{e}_i\delta t,t)\\
&=f_i^{\mathrm{eq}}-\delta t e_{i\alpha}\partial_\alpha f_i^{\mathrm{eq}}+\tfrac{1}{2}\delta t^2 e_{i\alpha}e_{i\beta}\partial_\alpha\partial_\beta f_i^{\mathrm{eq}}+O(\delta t^3). \qquad (32)
\end{aligned}
$$

The equilibrium distribution functions satisfy

$$
\begin{aligned}
\sum_i f_i^{\mathrm{eq}}=\rho,\ \sum_i f_i^{\mathrm{eq}}e_{i\alpha}=\rho_0 u_\alpha,\ &\sum_i f_i^{\mathrm{eq}}e_{i\alpha}e_{i\beta}\\
&=\rho c_s^2\delta_{\alpha\beta}+\rho_0 u_\alpha u_\beta,\\
\sum_i f_i^{\mathrm{eq}}e_{i\alpha}e_{i\beta}e_{i\gamma}=\rho_0 c_s^2(u_\alpha\delta_{\beta\gamma}+u_\beta\delta_{\alpha\gamma}&+u_\gamma\delta_{\alpha\beta}). \qquad (33)
\end{aligned}
$$

Substituting Eqs. (32) and (33) into Eqs. (28) and (29) and then combining Eqs. (30) and (31), the recovered macroscopic equations are

$$
\rho^{n+1}=\rho^n-\partial_\alpha(\rho_0 u_\alpha)^n\delta t+0.5\delta t^2\partial_\alpha\partial_\beta\big(\rho_0 u_\alpha u_\beta+\rho c_s^2\delta_{\alpha\beta}\big)^n, \qquad (34)
$$

$$
\begin{aligned}
(\rho_0 u_\alpha)^{n+1}=&(\rho_0 u_\alpha)^n-\partial_\beta\big(\rho_0 u_\alpha u_\beta+\rho c_s^2\delta_{\alpha\beta}\big)^n\delta t\\
&+\upsilon\delta t\partial_\beta(\partial_\beta u_\alpha)^n+\rho_0 c_s^2\delta t^2\partial_\beta(\partial_\gamma u_\gamma\delta_{\alpha\beta})^n. \qquad (35)
\end{aligned}
$$

It can be seen that they contain a mass diffusion term and a bulk viscosity term.

D. Analysis of LBFS

LBFS [16] is a finite-volume solver that uses the solution of a simplified LBE to calculate face fluxes. First, a unit lattice is constructed at the finite-volume cell face, and LBE with $\tau=1$ is used to obtain predicted variables at the cell face:

$$
\rho(\mathbf{x}_s,t+\delta t)=\sum_i f_i^{\mathrm{eq}}(\mathbf{x}_s-\mathbf{e}_i\delta t,t), \qquad (36)
$$

$$
(\rho u_\alpha)(\mathbf{x}_S,t+\delta t)=\sum_i e_{i\alpha}f_i^{\mathrm{eq}}(\mathbf{x}_s-\mathbf{e}_i\delta t,t). \qquad (37)
$$

Then $f_i^{\mathrm{eq}}(\mathbf{x}_S,t+\delta t)$ can be determined by Eq. (8).

Second, the mass flux P_α and momentum flux $\Pi_{\alpha\beta}$ at the cell face are calculated by

$$
P_\alpha=e_{i\alpha}f_i^{\mathrm{eq}}(\mathbf{x}_S,t+\delta t), \qquad (38)
$$

$$
\begin{aligned}
\Pi_{\alpha\beta}=&e_{i\alpha}e_{i\beta}f_i^{\mathrm{eq}}(\mathbf{x}_S,t+\delta t)+(0.5-\tau)e_{i\alpha}e_{i\beta}\\
&\times\big[f_i^{\mathrm{eq}}(\mathbf{x}_S,t+\delta t)-f_i^{\mathrm{eq}}(\mathbf{x}_S-\mathbf{e}_i\delta t,t)\big], \qquad (39)
\end{aligned}
$$

and the variables are updated by

$$
\partial_t\rho=-\frac{1}{\Delta V}\sum_k P_\alpha\Delta S_k n_{k\alpha}, \qquad (40)
$$

$$
\partial_t(\rho u_\alpha)=-\frac{1}{\Delta V}\sum_k \Pi_{\alpha\beta}\Delta S_k n_{k\beta}, \qquad (41)
$$

where ΔV is the volume of the finite-volume cell, ΔS_k is the area of the kth face, and $n_{k\alpha}$ is the outward normal of the kth face.

The recovered macroscopic equations with actual numerical dissipation terms of LBFS [24] are

$$
\rho^*=\rho^n-\partial_\alpha(\rho u_\alpha)^n\delta t+0.5\delta t^2\partial_\alpha\partial_\beta\big(\rho u_\alpha u_\beta+\rho c_s^2\delta_{\alpha\beta}\big)^n, \qquad (42)
$$

$$
\begin{aligned}
(\rho u_\alpha)^*=&-\partial_\beta\big(\rho u_\alpha u_\beta+\rho c_s^2\delta_{\alpha\beta}\big)^n\delta t\\
&+\tfrac{1}{2}c_s^2\delta t^2\partial_\beta\big[\partial_\beta(\rho u_\alpha)+2\partial_\gamma(\rho u_\gamma)\delta_{\alpha\beta}\big]^n, \qquad (43)
\end{aligned}
$$

$$
\partial_t\rho=-\partial_\alpha(\rho u_\alpha)^*, \qquad (44)
$$

$$
\begin{aligned}
\partial_t(\rho u_\alpha)=&-\partial_\beta\big(\rho u_\alpha u_\beta+\rho c_s^2\delta_{\alpha\beta}\big)\\
&+\upsilon\partial_\beta[\partial_\beta(\rho u_\alpha)+\partial_\beta(\rho u_\alpha)+\partial_\gamma(\rho u_\gamma)\delta_{\alpha\beta}]\\
&+(\tau-1.5)\big[\partial_\beta\big(\rho u_\alpha u_\beta+\rho c_s^2\delta_{\alpha\beta}\big)^*\\
&-\partial_\beta\big(\rho u_\alpha u_\beta+\rho c_s^2\delta_{\alpha\beta}\big)\big]. \qquad (45)
\end{aligned}
$$

Substituting Eqs. (42) and (43) into Eqs. (44) and (45), the final second-order macroscopic equations are

$$
\begin{aligned}
\partial_t\rho=&-\partial_\alpha(\rho u_\alpha)+\delta t\partial_\alpha\partial_\beta\big(\rho u_\alpha u_\beta+\rho c_s^2\delta_{\alpha\beta}\big)\\
&+1.5c_s^2\delta t^2\partial_\beta\partial_\beta\partial_\alpha(\rho u_\alpha), \qquad (46)
\end{aligned}
$$

$$
\begin{aligned}
\partial_t(\rho u_\alpha)=&-\partial_\beta\big(\rho u_\alpha u_\beta+\rho c_s^2\delta_{\alpha\beta}\big)\\
&+\upsilon\partial_\beta[\partial_\beta(\rho u_\alpha)+\partial_\beta(\rho u_\alpha)+\partial_\gamma(\rho u_\gamma)\delta_{\alpha\beta}]\\
&+(\tau-1.5)[\partial_\beta(\rho u_\alpha u_\beta)^*-\partial_\beta(\rho u_\alpha u_\beta)]\\
&+(\tau-1.5)c_s^2\delta t\partial_\alpha\big[-\partial_\beta(\rho u_\beta)\\
&+0.5\delta t\partial_\alpha\partial_\beta\big(\rho u_\alpha u_\beta+\rho c_s^2\delta_{\alpha\beta}\big)\big]. \qquad (47)
\end{aligned}
$$

It can be seen that they contain mass diffusion and additional bulk viscosity terms.

E. Analysis of LWACM

The LWACM without forcing term consists of three steps,

$$
\begin{aligned}
f_i^*(\mathbf{x}-\mathbf{e}_i\delta t,t)=&f_i^{\mathrm{eq}}(\mathbf{x}-\mathbf{e}_i\delta t,t)-(1-\tau)\\
&\times\big[f_i^{\mathrm{eq}}(\mathbf{x}-\mathbf{e}_i\delta t,t)-f_i^{\mathrm{eqo}}(\mathbf{x}-\mathbf{e}_i\delta t,t)\big], \qquad (48)
\end{aligned}
$$

$$
f_i^{**}(\mathbf{x},t+\delta t)=f_i^*(\mathbf{x}-\mathbf{e}_i\delta t,t), \qquad (49)
$$

$$
\begin{aligned}
f_i(\mathbf{x},t+\delta t)=&f_i^{**}(\mathbf{x},t+\delta t)\\
&+(1-\tau)\big[f_i^{\mathrm{eq}}(\mathbf{x},t)-f_i^{\mathrm{eqo}}(\mathbf{x},t)\big], \qquad (50)
\end{aligned}
$$

where f_i^{eq} is the same as that of the LBM, Eq. (8), and f_i^{eqo} is the oppsite equilibrium distribution function defined as

$$
f_i^{\mathrm{eqo}}=w_i\rho\left\{1+\frac{e_{i\alpha}(-u_\alpha)}{c_s^2}+\frac{[e_{i\alpha}(-u_\alpha)]^2}{2c_s^4}-\frac{(-u_\alpha)^2}{2c_s^2}\right\}. \qquad (51)
$$

It is easy to prove that f_i^{eqo} satisfies

$$
\begin{aligned}
\sum_i f_i^{\mathrm{eqo}}=\rho,\ \sum_i f_i^{\mathrm{eqo}}e_{i\alpha}=-\rho u_\alpha,\ &\sum_i f_i^{\mathrm{eqo}}e_{i\alpha}e_{i\beta}\\
&=\rho c_s^2\delta_{\alpha\beta}+\rho u_\alpha u_\beta,\\
\sum_i f_i^{\mathrm{eqo}}e_{i\alpha}e_{i\beta}e_{i\gamma}=-\rho c_s^2(u_\alpha\delta_{\beta\gamma}+u_\beta\delta_{\alpha\gamma}&+u_\gamma\delta_{\alpha\beta}). \qquad (52)
\end{aligned}
$$

The macroscopic variables ρ, ρu_α, and υ are determined by Eqs. (10)–(12), respectively.

Combining Eqs. (48)–(50), the evolution equation of the distribution function can be rewritten as

$$\begin{aligned} f_i(\mathbf{x}, t+\delta t) = {}& \tau f_i^{\mathrm{eq}}(\mathbf{x}-\mathbf{e}_i\delta t, t) + (1-\tau) f_i^{\mathrm{eqo}}(\mathbf{x}-\mathbf{e}_i\delta t, t) \\ & + (1-\tau)\big[f_i^{\mathrm{eq}}(\mathbf{x}, t) - f_i^{\mathrm{eqo}}(\mathbf{x}, t)\big]. \end{aligned} \tag{53}$$

Expanding $f_i^{\mathrm{eq}}(\mathbf{x}-\mathbf{e}_i\delta t, t)$ and $f_i^{\mathrm{eqo}}(\mathbf{x}-\mathbf{e}_i\delta t, t)$ with a second-order Taylor series expansion leads to

$$\begin{aligned} f_i^{\mathrm{eq}}(\mathbf{x}-\mathbf{e}_i\delta t, t) = {}& f_i^{\mathrm{eq}} - \delta t e_{i\alpha}\partial_\alpha f_i^{\mathrm{eq}} \\ & + \tfrac{1}{2}\delta t^2 e_{i\alpha}e_{i\beta}\partial_\alpha\partial_\beta f_i^{\mathrm{eq}} + O(\delta t^3), \end{aligned} \tag{54}$$

$$\begin{aligned} f_i^{\mathrm{eqo}}(\mathbf{x}-\mathbf{e}_i\delta t, t) = {}& f_i^{\mathrm{eqo}} - \delta t e_{i\alpha}\partial_\alpha f_i^{\mathrm{eqo}} \\ & + \tfrac{1}{2}\delta t^2 e_{i\alpha}e_{i\beta}\partial_\alpha\partial_\beta f_i^{\mathrm{eqo}} + O(\delta t^3). \end{aligned} \tag{55}$$

Substituting Eqs. (54) and (55) into (53) leads to

$$\begin{aligned} f_i(\mathbf{x}, t+\delta t) = {}& \tau\big[f_i^{\mathrm{eq}} - \delta t e_{i\alpha}\partial_\alpha f_i^{\mathrm{eq}} \\ & + \tfrac{1}{2}\delta t^2 e_{i\alpha}e_{i\beta}\partial_\alpha\partial_\beta f_i^{\mathrm{eq}} + O(\delta t^3)\big]. \\ & + (1-\tau)\big[f_i^{\mathrm{eqo}} - \delta t e_{i\alpha}\partial_\alpha f_i^{\mathrm{eqo}} \\ & + \tfrac{1}{2}\delta t^2 e_{i\alpha}e_{i\beta}\partial_\alpha\partial_\beta f_i^{\mathrm{eqo}} + O(\delta t^3)\big] \\ & + (1-\tau)\big(f_i^{\mathrm{eq}} - f_i^{\mathrm{eqo}}\big) \end{aligned} \tag{56}$$

Taking summation of Eq. (56) over index i, we can obtain

$$\begin{aligned} \rho^{n+1} = {}& \rho^n - (2\tau-1)\delta t\partial_\alpha(\rho u_\alpha)^n \\ & + 0.5\delta t^2\partial_\alpha\partial_\beta\big(\rho u_\alpha u_\beta + \rho c_s^2\delta_{\alpha\beta}\big)^n. \end{aligned} \tag{57}$$

Multiplying both sides of Eq. (56) with $\mathbf{e}_i$ and then making summation over index i, we can obtain the macroscopic momentum equation:

$$\begin{aligned} (\rho u_\alpha)^{n+1} = {}& (\rho u_\alpha)^n - \delta t\partial_\beta\big(\rho u_\alpha u_\beta + \rho c_s^2\delta_{\alpha\beta}\big) \\ & + \upsilon\delta t\partial_\beta[\partial_\beta(\rho u_\alpha) + \partial_\alpha(\rho u_\beta) + \partial_\gamma(\rho u_\gamma)\delta_{\alpha\beta}]. \end{aligned} \tag{58}$$

The mass diffusion term in the density equation and the bulk viscosity term in the momentum equation can also be found here.

F. Summary

From the analyses of five weakly compressible models, it can be seen that all models contain mass diffusion terms related to $\partial_\alpha\partial_\alpha\rho$ in the continuity equation and bulk viscosity terms related to $\partial_\alpha(\partial_\beta u_\beta)$ in the momentum equation. Especially, the additional terms in the macroscopic equations of the FSLBM include only the mass diffusion and bulk viscosity terms. And it has been proven that in the simplified MAMEs [21], both the additional terms in the density equation (mass diffusion term) and momentum equation (bulk viscosity term) are effective in stabilizing computation. These results imply that the mass diffusion and bulk viscosity terms provide general mechanisms for stabilizing the computation of weakly compressible models.

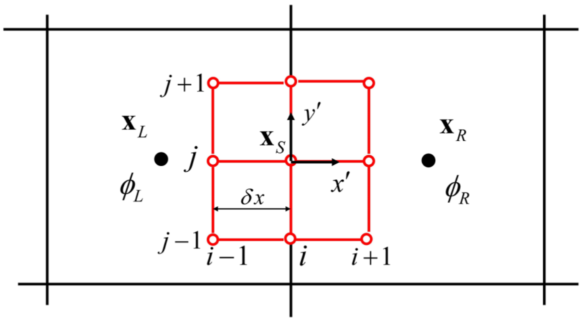

FIG. 1. The reconstructed unit lattice at the finite-volume cell face.

It should be noticed that compared with LBM, both MAMEs and the simplified MAMEs can only maintain numerical stability for small τ ($\tau < 0.88$ for MAMEs and $\tau < 1.16$ for the simplified MAMEs) [21]. The reason for the good numerical stability of LBM at large τ still needs to be explored.

As to SLBM and LBFS, only equilibrium distribution functions are involved, which implies that they are intrinsically macroscopic models. The two models also show good numerical stability at high Re (small τ) and limited numerical stability at low Re (large τ) [19,24]. The derived macroscopic equations of SLBM [19] and LBFS [24] can recover the numerical stability and accuracy of the original models very well. FSLBM and LWACM only contain equilibrium distribution functions; thus, their numerical stability and accuracy can be recovered by the derived macroscopic equations as well.

III. GENERAL WEAKLY COMPRESSIBLE SOLVER FOR ISOTHERMAL FLOW AND VALIDATION OF THE GENERAL MECHANISMS

Referring to the general mechanisms and the computational procedures of LBFS, a general weakly compressible solver for isothermal flows, abbreviated as GWCSIF, is proposed.

A. Construction of GWCSIF

The detailed procedures of GWCSIF are summarized as follows:

(a) A unit lattice is constructed at the finite-volume cell face, as shown in Fig. 1. For 2D cases, a 3 × 3 unit lattice is adopted, and for 3D cases, a 3 × 3 × 3 unit lattice is adopted. It should be noted that the unit lattice is based on a local coordinate to ensure lattice symmetry about the face. Variables at the lattice nodes are interpolated by

$$\phi = \begin{cases} \phi_L + \nabla\phi_L\cdot(\mathbf{x}_S - \mathbf{e}_i\delta t - \mathbf{x}_L) \ \ \mathbf{x}_S - \mathbf{e}_i\delta t & \text{at the left cell} \\ \phi_R + \nabla\phi_R\cdot(\mathbf{x}_S - \mathbf{e}_i\delta t - \mathbf{x}_R) \ \ \mathbf{x}_S - \mathbf{e}_i\delta t & \text{at the right cell} \\ 0.5[\phi_L + \nabla\phi_L\cdot(\mathbf{x}_S - \mathbf{e}_i\delta t - \mathbf{x}_L) + \phi_R + \nabla\phi_R\cdot(\mathbf{x}_S - \mathbf{e}_i\delta t - \mathbf{x}_R)] \ \ \mathbf{x}_S - \mathbf{e}_i\delta t & \text{at the interface} \end{cases}. \tag{59}$$

where ϕ denotes an arbitrary variable; subscripts S, L, and R denote the variables at the face, left cell, and right cell, respectively. The partial derivatives at the cell centers are calculated by the Green-Gauss gradient scheme:

$$\Delta V \partial_\alpha \phi = \sum_k \phi_s \Delta S_k n_{k\alpha}. \tag{60}$$

The macroscopic variables at the face in Eq. (60) are obtained by a linearized interpolation:

$$\phi_S = \frac{\phi_L |\mathbf{x}_R - \mathbf{x}_s|}{|\mathbf{x}_R - \mathbf{x}_s| + |\mathbf{x}_L - \mathbf{x}_s|} + \phi_R \left(1 - \frac{|\mathbf{x}_R - \mathbf{x}_s|}{|\mathbf{x}_R - \mathbf{x}_s| + |\mathbf{x}_L - \mathbf{x}_s|} \right). \tag{61}$$

(b) Predictor step. With the interpolated variables on lattice nodes, the governing equations are solved on the unit lattice to obtain the predicted variables at $\mathbf{x}_S$. The discretized equations are

$$\rho^* = \rho^n - \partial_\alpha (\rho u_\alpha)^n \delta t, \tag{62}$$

$$\begin{aligned} (\rho u_\alpha)^* = {} & (\rho u_\alpha)^n - \delta t \partial_\beta \left(\rho u_\alpha u_\beta + \rho c_s^2 \delta_{\alpha\beta} \right)^n \\ & + \mu \delta t \partial_\beta (\partial_\beta u_\alpha + \partial_\alpha u_\beta)^n. \end{aligned} \tag{63}$$

The partial derivatives in Eqs. (62) and (63) are discretized by the least-squares finite-difference method. More details can be seen in Ref. [19].

(c) Corrector step. The interface mass flux P_α and momentum flux $\Pi_{\alpha\beta}$ are obtained by

$$P_\alpha = (\rho u_\alpha)^*, \tag{64}$$

$$\Pi_{\alpha\beta} = \partial_\beta \left(\rho u_\alpha u_\beta + \rho c_s^2 \delta_{\alpha\beta} \right)^* - \mu \partial_\beta (\partial_\beta u_\alpha + \partial_\alpha u_\beta)^n, \tag{65}$$

where the first-order partial derivatives at time step n are adopted to simplify computation. The variables are updated by

$$\frac{\partial \rho}{\partial t} = -\frac{1}{\Delta V} \sum_k P_\alpha \Delta S_k n_{k\alpha}, \tag{66}$$

$$\frac{\partial (\rho u)}{\partial t} = \frac{-1}{\Delta V} \sum_k \prod_{\alpha\beta} \Delta S_k n_{k\beta}. \tag{67}$$

Substituting Eqs. (62) and (63) into Eqs. (66) and (67), the macroscopic equations of GWCSIF can be given as

$$\begin{aligned} \frac{\partial \rho}{\partial t} = {} & -\partial_\alpha (\rho u_\alpha) + \delta t \partial_\alpha \partial_\beta \left(\rho u_\alpha u_\beta + \rho c_s^2 \delta_{\alpha\beta} \right) \\ & - \delta t \partial_\alpha \partial_\beta [\mu (\partial_\alpha u_\beta + \partial_\beta u_\alpha)], \end{aligned} \tag{68}$$

$$\begin{aligned} \frac{\partial (\rho u_\alpha)}{\partial t} = {} & -\partial_\beta (\rho u_\alpha u_\beta)^* - \partial_\beta \left(\rho c_s^2 \delta_{\alpha\beta} \right) \\ & + c_s^2 \delta t \partial_\alpha [\partial_\beta (\rho u_\beta)] + \partial_\beta [\mu (\partial_\beta u_\alpha + \partial_\alpha u_\beta)]^n. \end{aligned} \tag{69}$$

It can be seen that by adopting the computational procedures of LBFS, the mass diffusion and bulk viscosity terms are introduced implicitly. It should be noted that the procedures are based on the standard governing equations and thus can be extended to construct other weakly compressible models. The generality can be shown in the construction of GWCSTF (see Sec. V).

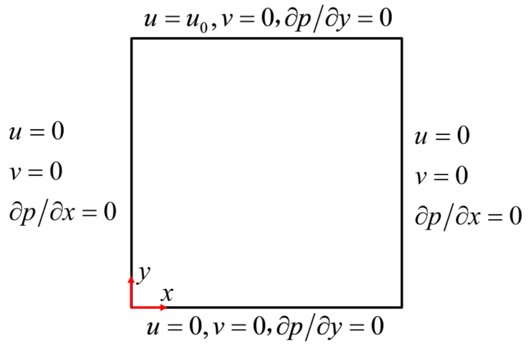

FIG. 2. Schematic of 2D lid-driven cavity flow.

As to the boundary treatment, ghost cells are adopted. Thus, the boundary fluxes can be computed using the abovementioned procedures.

B. Dissipative model

The dissipative model based on the least-squares-based finite-difference method is proposed to validate the general mechanisms that do not rely on discretization schemes. The governing equations of the dissipative model are the governing equations with the two general dissipation terms:

$$\frac{\partial \rho}{\partial t} = -\partial_\alpha (\rho u_\alpha) + \delta t \partial_\alpha \partial_\beta \left(\rho c_s^2 \delta_{\alpha\beta} \right), \tag{70}$$

$$\begin{aligned} \frac{\partial (\rho u_\alpha)}{\partial t} = {} & -\partial_\beta (\rho u_\alpha u_\beta) - \partial_\beta \left(\rho c_s^2 \delta_{\alpha\beta} \right) \\ & + \rho c_s^2 \delta t \partial_\alpha (\partial_\beta u_\beta) + \partial_\beta [\mu (\partial_\beta u_\alpha + \partial_\alpha u_\beta)]^n. \end{aligned} \tag{71}$$

Here, the coefficients of the mass diffusion and bulk viscosity terms refer to those of GWCSTF, Eqs. (68) and (69). The partial derivatives of space are discretized by the least-squares finite-difference method. More details can be seen in Ref. [19].

C. Validation of the general mechanisms

To validate the general mechanisms for stabilizing computation, the numerical stability of GWCSIF, the dissipative model, and other weakly compressible models is investigated by simulating the 2D lid-driven cavity flow at different mesh sizes and Reynolds numbers. In the present paper, GWCSTF, LBFS, and the dissipative model are discretized with the explicit first-order scheme to clarify the general mechanisms.

The physical model is depicted in Fig. 2. The cavity of size $L \times L$ is filled with fluid. The lid has a constant horizontal velocity $u_0 = 0.1$, and the other three walls are stationary. The problem is characterized by the Reynolds number defined as $\mathrm{Re} = (u_0 L)/\upsilon$. The convergence criterion is

$$\frac{\sum_{i,j} \left| \left| \mathbf{u}_{i,j}^{n+1} \right| - \left| \mathbf{u}_{i,j}^{n} \right| \right|}{\sum_{i,j} \left| \mathbf{u}_{i,j}^{n+1} \right|} \leqslant 10^{-8}. \tag{72}$$

First, the weakly compressible models based on the finite-difference scheme, LBM, SLBM, FSLBM, LWACM, and the

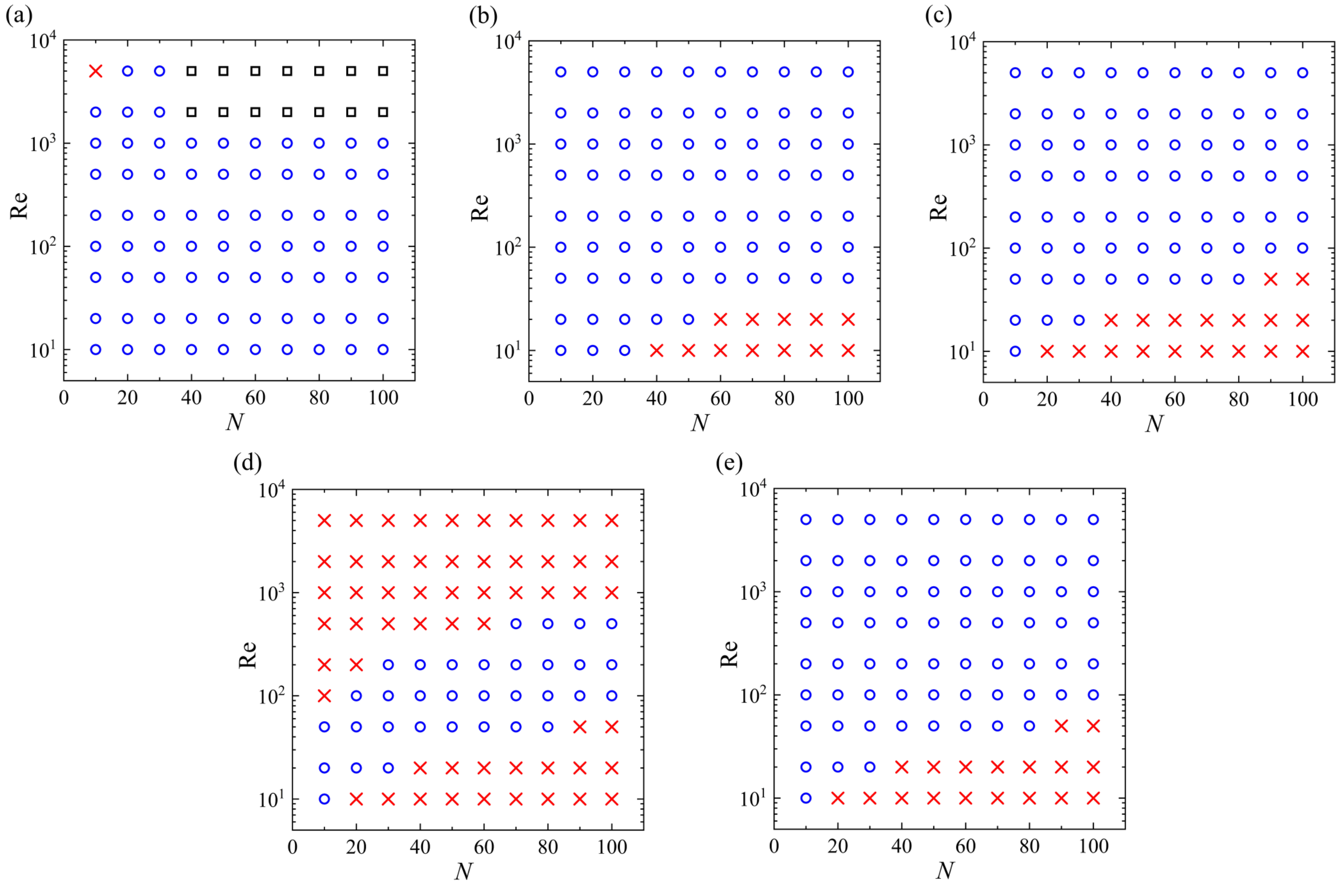

FIG. 3. Numerical stability tests for LBM (a), SLBM (b), FSLBM (c), LWACM (d), and the dissipative model (e) at different mesh sizes and Re, where N is the mesh number in length L. The blue circle represents convergence, the red cross represents divergence, and the black square represents the results that do not converge but also cannot meet the convergence criteria.

dissipative model, are investigated. The LBM here adopts the nonequilibrium extrapolation boundary condition [25] for all boundaries owing to its generality and good numerical stability. The predictor and corrector time steps of the dissipative model are $\delta t = 0.5$ and $\Delta t = 1$, respectively, and the time steps for other models are 1.

The results of numerical stability are summarized in Fig. 3. It can be seen that the stable parameter ranges of SLBM, FSLBM, and the dissipative model have the same characteristic. Both of them show good numerical stability at small υ, while there is instability at large υ. The result implies that the general mechanisms can well explain the good numerical stability of SLBM and FSLBM.

For LWACM, it shows instability at large υ, and also at very small υ. It is due to the fact that LWACM adopts a sound speed $c_s\sqrt{(2\tau-1)}$. The general mechanisms indeed contribute to stabilizing computation. However, at small υ (τ approaches 0.5), the Mach number $u_0/\sqrt{(2\tau-1)}c_s$ exceeds the incompressible limit of 0.3 and makes the model divergent.

As for LBM, it has intrinsic mechanisms beyond the general mechanisms to stabilize computations at large υ. However, its numerical stability at small υ is worse than the dissipative model with the general mechanisms.

Second, the two weakly compressible models based on the finite-volume scheme, LBFS, and GWCSIF, are investigated. The predictor and corrector time steps of the two models are $\delta t = 0.5$ and $\Delta t = 0.5$, respectively. As shown in Fig. 4, both GWCSIF and LBFS exhibit good numerical stability for $\upsilon \leqslant 0.25$. They can retain stability at $\mathrm{Re} = 5000$ even for a very coarse mesh 10×10. Also, the stable parameter ranges of the two methods are similar. The result indicates that GWCSIF can achieve good numerical stability for high Reynolds number flows by adopting the general mechanisms for stabilizing computation. The good numerical stability of LBFS can be well explained by the general mechanisms. For low Reynolds number flows, a smaller υ can be adopted to ensure numerical stability.

IV. NUMERICAL TESTS FOR INCOMPRESSIBLE ISOTHERMAL FLOW

Four numerical tests are conducted in this section to test the accuracy and correctness of GWCSIF. The sound speed $c_s = 1/\sqrt{3}$ is adopted for all cases.

A. Taylor-Green vortex flow

To compare the accuracy of GWCSIF and LBFS, the two-dimensional Taylor-Green vortex flows with an analytical

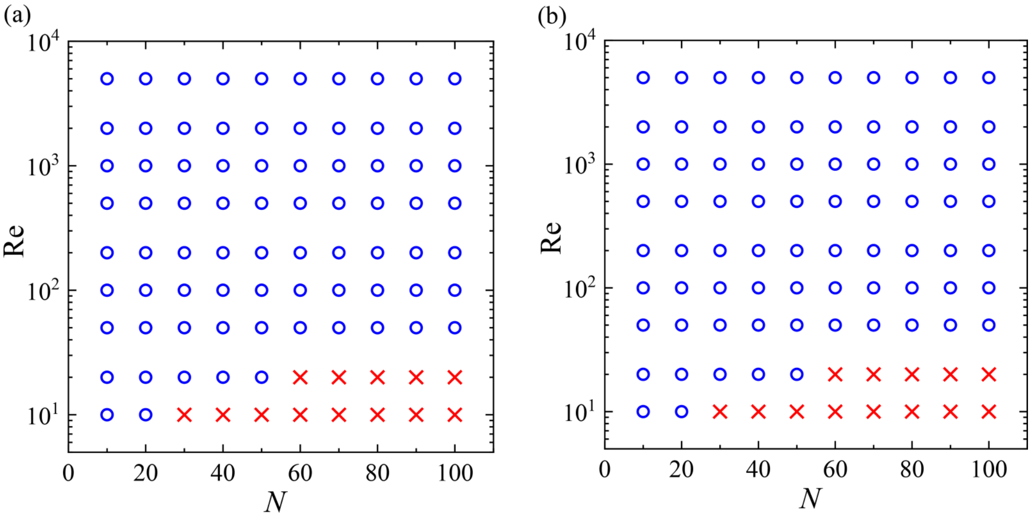

FIG. 4. Numerical stability tests for GWCSIF (a) and LBFS (b) at different mesh sizes and Re, where N is the mesh number in length L. The blue circle represents convergence, and the red cross represents divergence.

solution is simulated. The analytical solution is

$$u(x, y, t) = -u_0 \cos(\pi x/L) \sin(\pi y/L) \exp\left(-\frac{2\pi^2 u_0 t}{\mathrm{Re} L}\right), \tag{73a}$$

$$v(x, y, t) = u_0 \sin(\pi x/L) \cos(\pi y/L) \exp\left(-\frac{2\pi^2 u_0 t}{\mathrm{Re} L}\right), \tag{73b}$$

$$p(x, y, t) = p_0 - \frac{\rho_0 u_0^2}{4}[\cos(2\pi x/L) + \cos(2\pi y/L)] \times \exp\left(-\frac{4\pi^2 u_0 t}{\mathrm{Re} L}\right), \tag{73c}$$

where u_0 is the reference velocity, ρ_0 is the fluid density, p_0 is the reference pressure, and Re is the Reynolds number defined as $\mathrm{Re} = (u_0 L)/\upsilon$. The computational area is $-L \leqslant x \leqslant L$ and $-L \leqslant y \leqslant L$, and the four boundaries are both periodic.

The numerical errors at different mesh sizes are investigated to compare the accuracy of GWCSIF and LBFS. The fixed parameters are $\Delta t = 0.5$, $\Delta x = 1$, $c_s=1/\sqrt{3}$, $\upsilon = 0.05$, and $\mathrm{Re} = 20$. The mesh has five different sizes, including 40×40, 60×60, 80×80, 100×100, and 120×120; δt has three values, $0.6\Delta t$, $0.8\Delta t$, and Δt. The numerical error is calculated at $t^* = u_0 t/L = 1$, and it is defined as

$$E_2 = \sqrt{\frac{\sum_{i=1}^{N\times N}[(u_n - u_a)/u_0]^2}{N \times N}}, \tag{74}$$

where u_n and u_a are the numerical results and analytical solutions, respectively.

Figure 5 implies that both GWCSIF and LBFS have second-order spatial accuracy. The numerical errors of GWCSIF are always close to those of LBFS, which indicates that GWCSIF and LBFS have similar numerical accuracy.

B. Viscous flow around a cylinder

To show the flexibility of GWCSIF for the curved boundary, viscous flow past a cylinder is simulated in this section. The schematic of the O-type mesh used in GWCSIF is shown in Fig. 6. The free-stream density and velocity are ρ_∞ and u_∞, respectively. The problem is characterized by the Reynolds number defined as $\mathrm{Re} = (u_\infty D)/\upsilon$, where D is the diameter of the cylinder.

First, steady flows at $\mathrm{Re} = 20$ and 40 are simulated. The corresponding ρ_∞ and u_∞ are 1 and $0.05c_s$, respectively. The computational domain is $0.5D \leqslant r \leqslant 25.5D$. The mesh size is 300×200, and the distance from the nearest computational node to the cylinder surface is $0.008D$. Initially, the pressure and velocity are set as the free-stream properties. For steady flow, the convergence criterion is

$$\frac{\sum ||\mathbf{u}|^{n+1} - |\mathbf{u}|^n|}{\sum |\mathbf{u}|^{n+1}} \leqslant 10^{-9}. \tag{75}$$

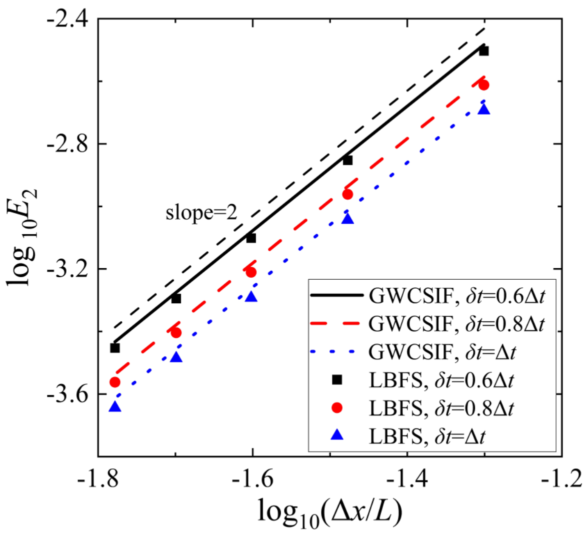

FIG. 5. Numerical errors of GWCSIF and LBFS at different mesh sizes and δt.

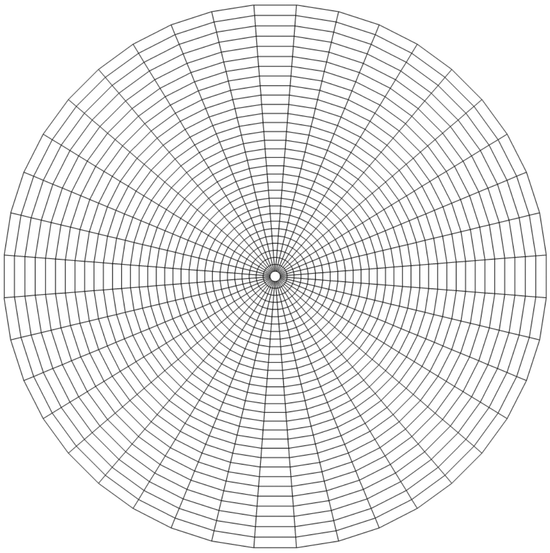

FIG. 6. Schematic of O-type mesh used in GWCSIF.

Four dimensionless parameters (the pressure coefficient C_p, drag coefficient C_d, lift coefficient C_l, and Strouhal number St) are used to quantify the results. Their definitions are

$$C_p = \frac{p_w - p(\rho_\infty)}{\frac{1}{2}\rho_\infty u_\infty^2}, \tag{76}$$

$$C_d = \frac{F_x}{\frac{1}{2}D\rho_\infty u_\infty^2}, \tag{77}$$

$$C_l = \frac{F_y}{\frac{1}{2}D\rho_\infty u_\infty^2}, \tag{78}$$

$$\mathrm{St} = f_s D/u_\infty, \tag{79}$$

where p_w is the pressure on the cylinder surface, f_s is the vortex shedding frequency, and F_x and F_y are the components of the total force acting on the cylinder. The total force is calculated by

$$F_\alpha = \int_A [-p\delta_{\alpha\beta} + \mu(\partial_\beta u_\alpha + \partial_\alpha u_\beta)]n_\beta dS. \tag{80}$$

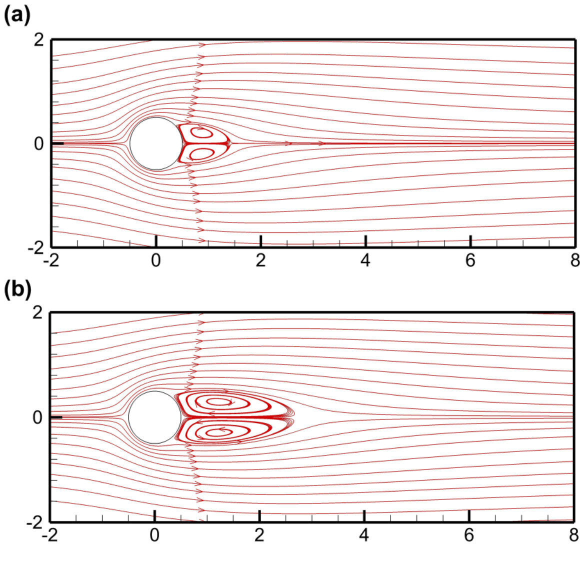

FIG. 7. Streamlines of viscid flow across a cylinder at Re = 20 (a) and 40 (b) obtained by GWCSIF.

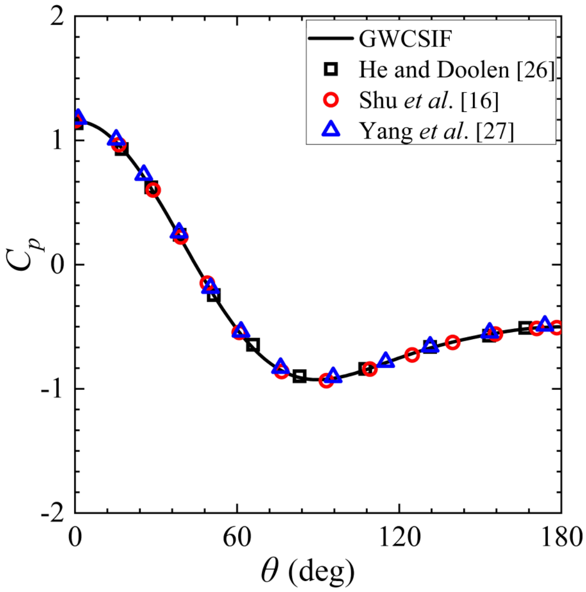

FIG. 8. C_p distribution on the cylinder surface at Re = 40, together with those given by He and Doolen [26], Shu *et al.* [16], and Yang *et al.* [27]. The orientation angle θ is measured from the leading stagnation point along the clockwise direction.

Figure 7 shows the steady flow fields around the cylinder at Re = 20 and 40. It can be seen that the two vortices behind the cylinder are symmetric, and their length extends with Re increasing from 20 to 40. To validate the results, Fig. 8 depicts the C_p profile at Re = 40 along the cylinder surface, together with those given by He and Doolen [26], Shu *et al.* [16], and Yang *et al.* [27]. It can be seen that the result obtained by GWCSIF is in good accordance with the reference results.

Furthermore, Table I compares drag coefficients C_d, recirculation lengths L_s, and separation angles θ_s obtained by GWCSIF with reference data. Good agreement can be observed.

For Re = 100 and 200, the flow is unsteady and finally becomes periodic. The corresponding ρ_∞ and u_∞ used in

TABLE I. Comparison of drag coefficients C_d, recirculation lengths L_s, and separation angles θ_s at Re = 20 and 40.

Re	References	C_d	L_s/D	θ_s
20	Dennis and Chang [28]	2.05	0.94	43.7
	Nieuwstadt and Keller [29]	2.053	0.893	43.37
	He and Doolen [26]	2.15	0.921	42.96
	Shu *et al.* [16]	2.062	0.935	42.94
	GWCSIF	2.062	0.913	43.70
40	Dennis and Chang [28]	1.52	2.35	53.8
	Nieuwstadt and Keller [29]	1.550	2.179	53.34
	He and Doolen [26]	1.499	2.245	52.84
	Shu *et al.* [16]	1.53	2.240	52.69
	GWCSIF	1.537	2.218	53.68

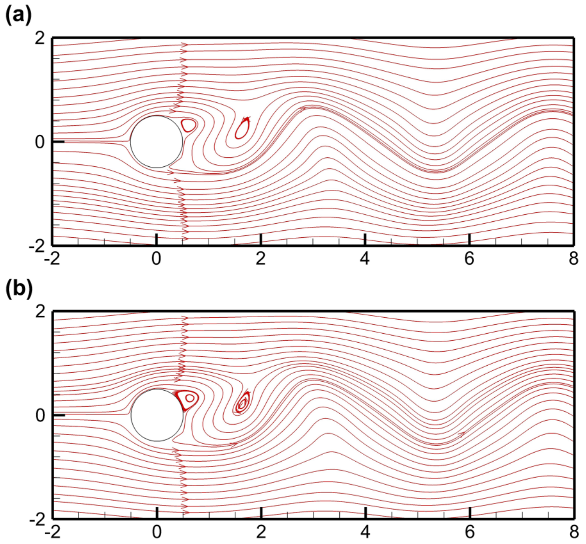

FIG. 9. Transient streamlines at Re = 100 (a) and 200 (b) given by GWCSIF.

simulations are 1 and $0.1c_s$, respectively. Figure 9 shows the transient flow fields around the cylinder. The vortices become asymmetric, and the Kármán vortex street can be observed. Figure 10 depicts the transient drag and lift coefficients. It can be seen that both drag and lift coefficients finally become periodic. To validate GWCSIF, C_d, C_l, and St at Re = 100 and 200 obtained by GWCSIF are compared with reference results. As shown in Table II, the results obtained by GWCSIF show good agreement with the reference results.

C. Inviscid flow across a cylinder

To show the good numerical stability of GWCSIF for high Reynolds number flows, an extreme case with an infinite Reynolds number, the inviscid flow across a cylinder, is simulated. The physical model is similar to that depicted in Sec. IV B. The cylinder surface is set as the nonpenetration boundary condition, while the free-stream properties are imposed on the outer boundary. The mesh size is 300 × 200, the computational domain is $0.5D \leqslant r \leqslant 25.5D$, and the distance from the nearest computational node to the cylinder surface is $0.008D$. The convergence criterion is

$$\frac{\sum ||\mathbf{u}|^{n+1} - |\mathbf{u}|^{n}|}{\sum |\mathbf{u}|^{n+1}} \leqslant 10^{-8}. \qquad (81)$$

TABLE II. Comparisons of C_d, C_l, and St at Re = 100 and 200 obtained by GWCSIF with reference results.

Re	References	C_d	C_l	St
100	Braza *et al.* [30]	1.28 ± 0.02	±0.30	0.16
	Liu *et al.* [31]	1.350 ± 0.012	±0.339	0.164
	Ding *et al.* [32]	1.325 ± 0.008	±0.28	0.164
	Shu *et al.* [16]	1.334 ± 0.009	±0.33	0.164
	GWCSIF	1.331 ± 0.009	±0.325	0.1644
200	Braza *et al.* [30]	1.38 ± 0.07	±0.78	0.190
	Liu *et al.* [31]	1.31 ± 0.049	±0.69	0.192
	Ding *et al.* [32]	1.327 ± 0.045	±0.60	0.196
	Shu *et al.* [16]	1.338 ± 0.045	±0.69	0.197
	GWCSIF	1.333 ± 0.0446	±0.679	0.1957

The pressure contours near the cylinder are shown in Fig. 11. It can be seen that the pressure field is symmetric about the line $x = 0$, which implies that the fluid does not have a pressure drop induced by the viscosity after crossing the cylinder. Figure 12 exhibits the streamlines around the cylinder. The streamlines flow smoothly across the cylinder and are symmetric about the line $x = 0$, which is a typical feature of the inviscid flow.

Furthermore, the pressure coefficient profile on the cylinder surface obtained by GWCSIF is compared with the theoretical result in Fig. 13. The theoretical pressure coefficient distribution is

$$C_p = 1 - 4(\sin\theta)^2, \qquad (82)$$

where the orientation angle θ is measured from the upstream stagnation point along the clockwise direction. It can be seen that the pressure coefficient profiles given by GWCSIF agree well with the theoretical solution. The successful simulation of inviscid flow validates the good numerical stability of GWCSIF at high Reynolds numbers.

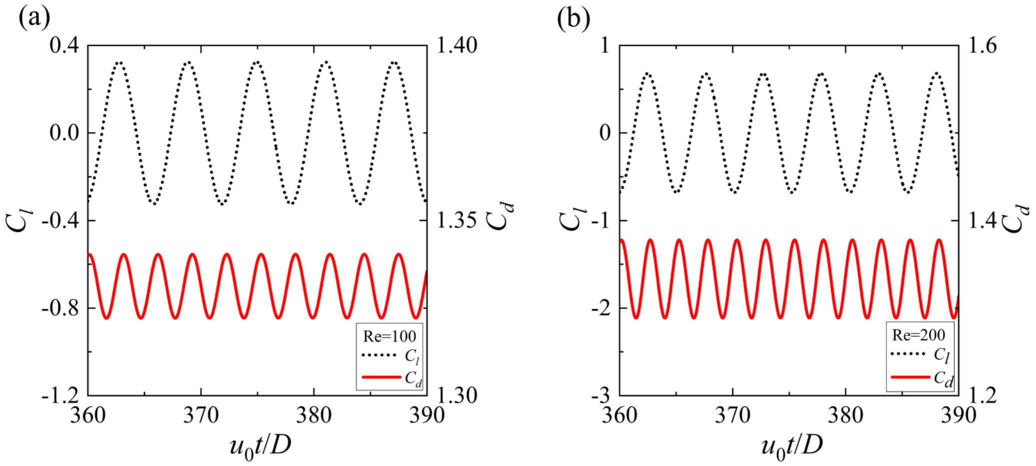

FIG. 10. Transient C_d and C_l at Re = 100 (a) and 200 (b) given by GWCSIF.

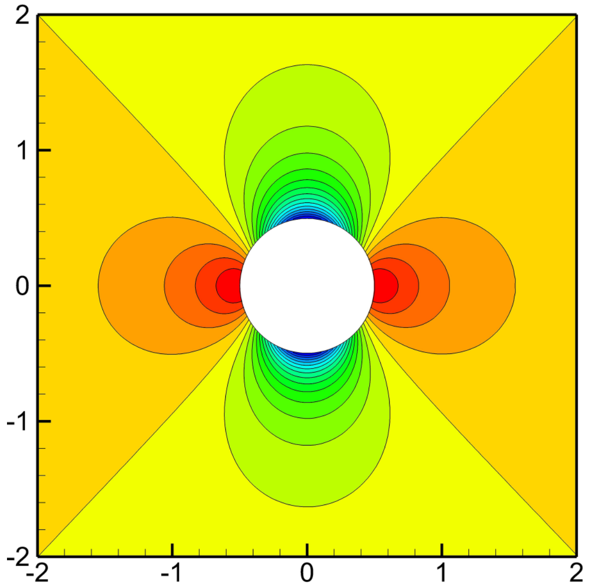

FIG. 11. Pressure contours of the inviscid flow past a circular cylinder given by GWCSIF.

D. 3D lid-driven cavity flow

The 3D lid-driven cavity flow is simulated to show the generality of GWCSIF for both 2D and 3D situations. The physical model shown in Fig. 14 is a cubic cavity of size $L{\times}L{\times}L$. The lid of the cavity has a constant velocity $(u_0, 0, 0)$ while other walls are stationary. The problem is characterized by the Reynolds number defined as $\mathrm{Re} = u_0 L/\upsilon$.

Three Reynolds numbers ($\mathrm{Re} = 100$, 400, and 1000) are considered in the present simulations. Nonuniform meshes are adopted, and the mesh sizes for $\mathrm{Re} = 100$, 400, and 1000 are $50 \times 50 \times 50$, $55 \times 55 \times 55$, and $60 \times 60 \times 60$, respectively. For all cases, $u_0 = 0.1c_s$ and $c_s = 1/\sqrt{3}$ are fixed.

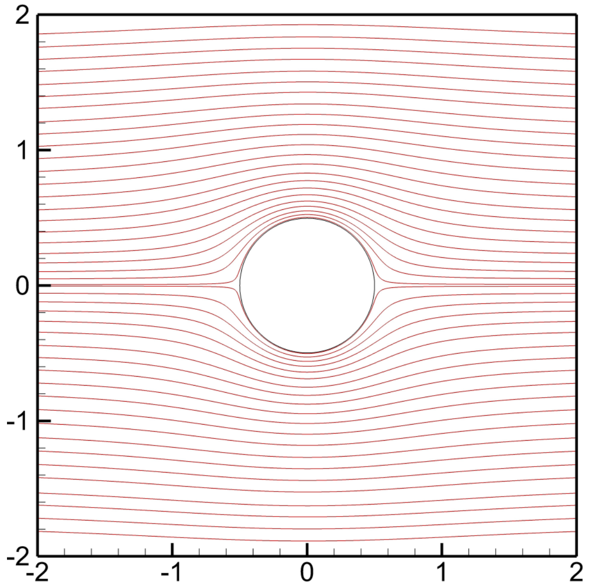

FIG. 12. Streamlines of the inviscid flow past a circular cylinder given by GWCSIF.

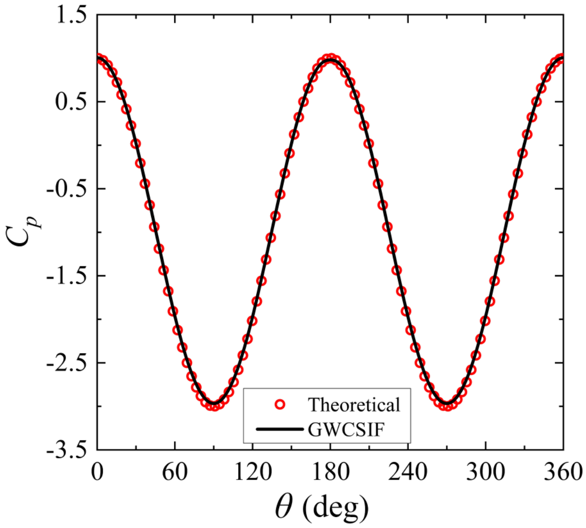

FIG. 13. Comparison of pressure coefficient distribution on the cylinder surface for inviscid flow across the cylinder.

To validate the results in quantity, u profiles along the line $x = 0.5L$, $y = 0.5L$, and w profiles along the line $y = 0.5L$, $z = 0.5L$ obtained by GWCSIF are compared with reference data in Fig. 15. The present results are in good accordance with reference results [33,34], which verifies the capability of GWCSIF for 3D simulations.

V. CONSTRUCTION AND ANALYSIS OF GENERAL WEAKLY COMPRESSIBLE SOLVERS FOR THERMAL FLOWS

A general approach to constructing general weakly compressible solvers has been proposed in Sec. III based on the general mechanisms for stabilizing computation. To show the

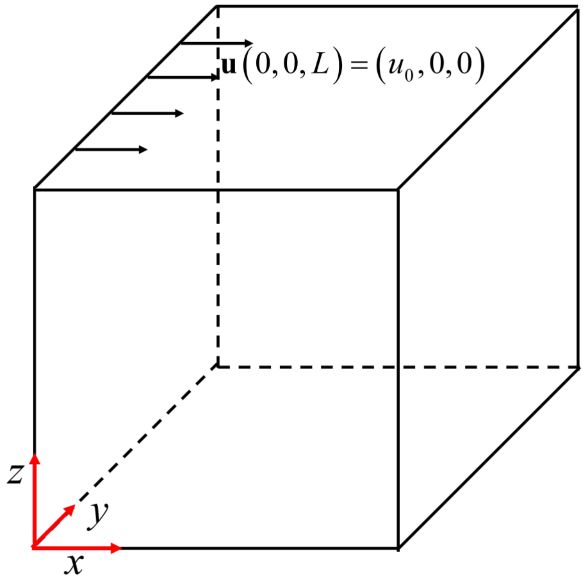

FIG. 14. Physical model of 3D lid-driven cavity flow.

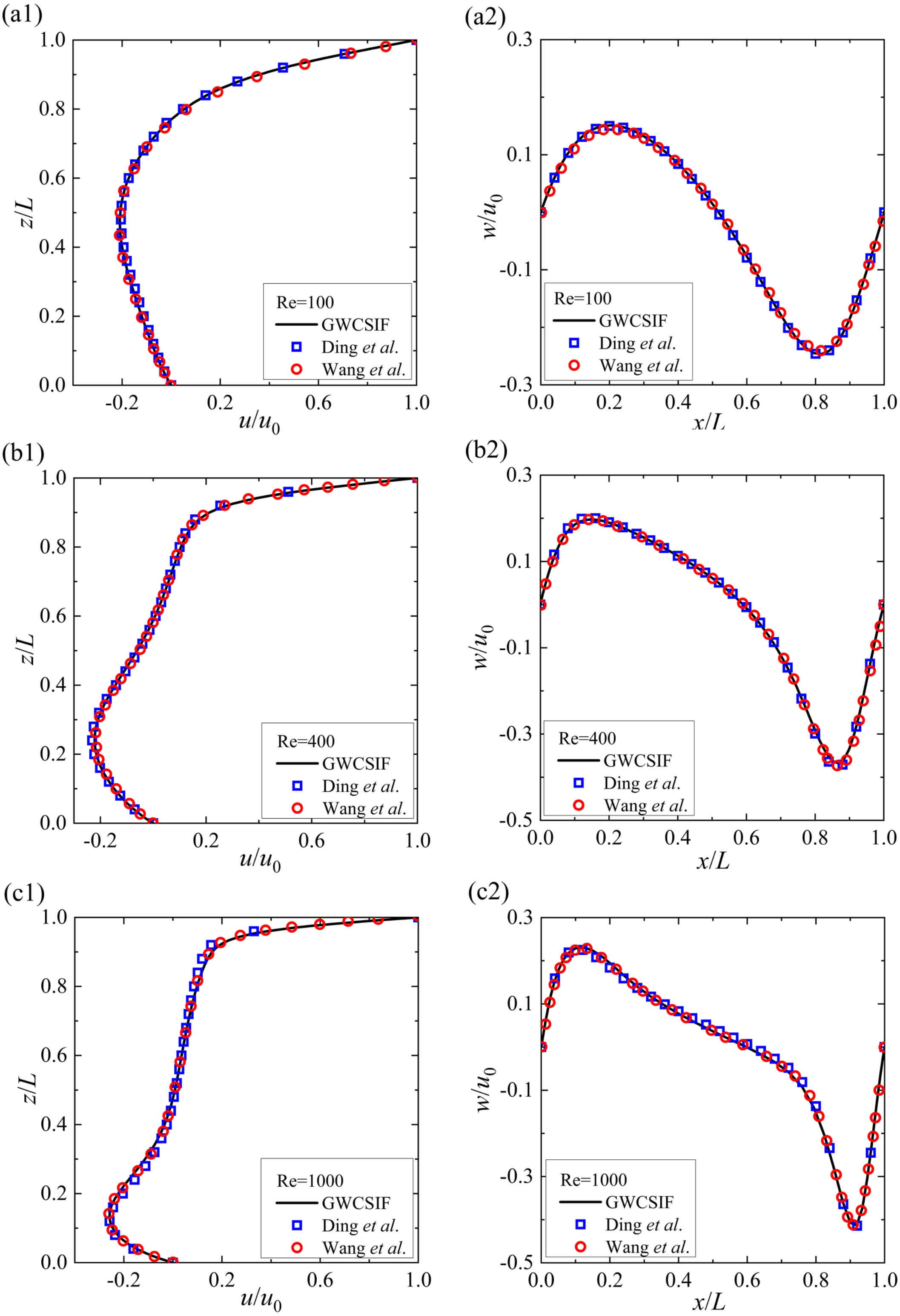

FIG. 15. u profiles along $x = 0.5L$, $y = 0.5L$, and w profiles along $y = 0.5L$, $z = 0.5L$ for 3D lid-driven cavity flow at Re = 100 (a1), (a2), 400 (b1), (b2), and 1000 (c1), (c2), together with the reference results given by Ding *et al.* [34] and Wang *et al.* [33].

generality of the approach, the general weakly compressible solver for incompressible thermal flows, labeled by GWCSTF, is proposed to simulate incompressible thermal flows.

A. Construction of GWCSTF

Like GWCSIF, GWCSTF can be directly constructed according to the governing equations. The governing equations

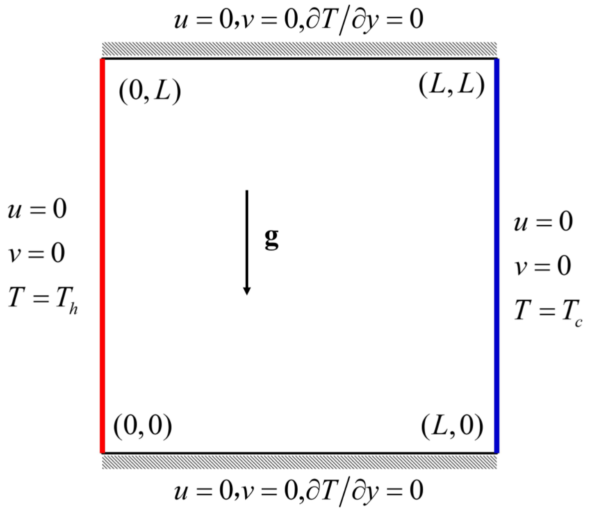

FIG. 16. Schematic of 2D lid-driven cavity flow.

for thermal flows are

$$\partial_t\rho + \partial_\alpha(\rho u_\alpha) = 0, \tag{83}$$

$$\partial_t(\rho u_\alpha) + \partial_\beta(\rho u_\alpha u_\beta) = -\partial_\alpha p + \mu\partial_\beta(\partial_\alpha u_\beta + \partial_\beta u_\alpha) + F_\alpha, \tag{84}$$

$$\partial_t(\rho c_p T) + \partial_\alpha(\rho c_p T u_\alpha) = \partial_\alpha(k\partial_\alpha T), \tag{85}$$

where k is the thermal conductivity, and c_p is the specific heat capacity at constant pressure.

The computational procedures of GWCSTF are summarized as follows:

(a) A unit lattice is constructed at the finite-volume cell face, which is the same as that of GWCSIF.

(b) Predictor step. The governing equations are solved on the unit lattice to obtain the predicted variables at the cell face. The discretized equations are

$$\rho^* = \rho^n - \partial_\alpha(\rho u_\alpha)^n\delta t, \tag{86}$$

$$(\rho u_\alpha)^* = (\rho u_\alpha)^n - \delta t\,\partial_\beta\big(\rho u_\alpha u_\beta + \rho c_s^2\delta_{\alpha\beta}\big)^n + \mu\delta t\,\partial_\beta(\partial_\beta u_\alpha + \partial_\alpha u_\beta)^n + F_\alpha^n\delta t, \tag{87}$$

$$(\rho c_p T)^* = (\rho c_p T)^n - \delta t\,\partial_\alpha(\rho c_p T u_\alpha)^n + \delta t\,\partial_\alpha(k\partial_\alpha T)^n. \tag{88}$$

Corrector step. The interface density flux P_α, momentum flux $\Pi_{\alpha\beta}$, and heat flux are obtained by

$$P_\alpha = (\rho u_\alpha)^*, \tag{89}$$

$$\Pi_{\alpha\beta} = \partial_\beta\big(\rho u_\alpha u_\beta + \rho c_s^2\delta_{\alpha\beta}\big)^* - \mu\partial_\beta(\partial_\beta u_\alpha + \partial_\alpha u_\beta)^n, \tag{90}$$

$$Q_\alpha = (\rho c_p T u_\alpha)^* - k(\partial_\alpha T)^n. \tag{91}$$

The variables are updated by

$$\frac{\partial\rho}{\partial t} = -\frac{1}{\Delta V}\sum_k P_\alpha\Delta S_k n_{k\alpha}, \tag{92}$$

$$\frac{\partial(\rho u_\alpha)}{\partial t} = \frac{-1}{\Delta V}\sum_k \Pi_{\alpha\beta}\Delta S_k n_{k\beta} + F_\alpha\delta t, \tag{93}$$

$$\frac{\partial(\rho c_p T)}{\partial t} = \frac{-1}{\Delta V}\sum_k Q_\alpha\Delta S_k n_{k\alpha}. \tag{94}$$

Similar to GWCSIF, the general numerical dissipation terms are introduced to GWCSTF implicitly.

For natural convection, the Boussinesq approximation is adopted, and the buoyancy is [35]

$$\mathbf{F} = \beta\mathbf{g}\rho(T - T_{\text{ref}}), \tag{95}$$

where T_{ref} is the reference temperature that can be chosen as the average temperature and $\mathbf{g}$ is the gravity acceleration.

B. Numerical stability test for GWCSTF

To test the numerical stability of GWCSTF, 2D natural convection in a square cavity is simulated. As shown in Fig. 16, the cavity of size $L \times L$ has four stationary walls. The temperatures of the left and right walls are set as T_h and T_l ($T_h > T_l$), respectively, and the upper and lower walls

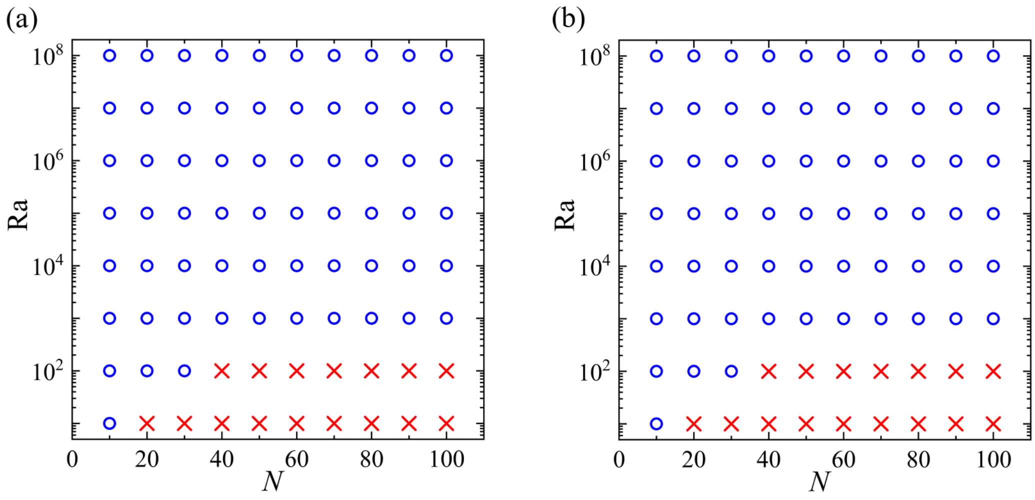

FIG. 17. Numerical stability of GWCSTF (a) and TLBFS (b) at different Ra and N. The blue circle represents convergence, while the red cross represents divergence.

are adiabatic. The problem is characterized by the Rayleigh number Ra and the Prandtl number Pr defined as

$$\mathrm{Ra} = \frac{\beta g(T_h - T_l)L^3}{\upsilon\chi} = \frac{V_c^2 L^2}{\chi\upsilon}, \quad \mathrm{Pr} = \frac{\upsilon}{\chi}, \tag{96}$$

where $V_c = \sqrt{\beta g(T_h - T_l)L}$ is the characteristic velocity and $\chi = k/(\rho c_p)$ is the thermal diffusivity. In present tests, $\mathrm{Pr} = 0.71$ and $V_c = 0.1$ are chosen.

The numerical stability of GWCSTF and thermal lattice Boltzmann flux solver [36] (TLBFS) at different Ra and N are investigated, where N is the mesh number for length L, and uniform meshes are used. TLBFS can be seen as the combination of LBFS for fluid flow and another solver for heat transfer. It also involves the general dissipation terms, according to the analysis for LBFS.

Other parameters are set as $\delta t = 0.5$, $\Delta t = 0.5$, and $V_c = 0.1$. As shown in Fig. 17, both GWCSTF and TLBFS have good numerical stability at high Ra. For $\mathrm{Ra} = 10^8$, their results are still stable even for a coarse mesh size of 10 × 10. In addition, the stable parameter ranges of GWCSTF and TLBFS show good agreement. The result indicates that by introducing the general numerical dissipation terms, both GWCSTF and TLBFS can achieve good numerical stability for high Ra flows.

VI. NUMERICAL TESTS FOR INCOMPRESSIBLE THERMAL FLOW

Three cases are simulated in this section to validate GWCSTF further.

A. Convection diffusion of a Gaussian hill

To test the accuracy of GWCSTF, the convection diffusion of a Gaussian hill is simulated. The computational domain is $[-2L, 2L] \times [-2L, 2L]$ and has a constant uniform velocity $\mathbf{u} = (u_0, 0)$. Initially, the temperature field is

$$T(\mathbf{x}, 0) = \frac{T_0}{2\pi\sigma^2} \exp\left[\frac{-(\mathbf{x} - \mathbf{x}_0)^2}{2\sigma^2}\right], \tag{97}$$

where $\sigma = 0.2L$, $T_0 = 2\pi\sigma^2$, and $x_0 = (-L, 0)$. The analytical solution is

$$T(\mathbf{x}, t) = \frac{T_0}{2\pi(2\chi t + \sigma^2)} \exp\left[\frac{-(\mathbf{x} - \mathbf{x}_0 - \mathbf{u}t)^2}{2(2\chi t + \sigma^2)}\right]. \tag{98}$$

The periodic boundary condition is adopted for all boundaries, and the simulation time is short enough to avoid the error induced by the finite computational domain.

The temperature field at the Fourier number $\mathrm{Fo} = t\chi/L^2 = 0.02$ is outputted and compared with the corresponding analytical solutions. A uniform mesh of size 200 × 200 is adopted, and other parameters are $\delta t = 0.5$, $\Delta t = 0.5$, the Péclet number $\mathrm{Pe} = u_0 L/\chi = 20$, and the mesh Fourier number $\mathrm{Fo}_{\Delta x} = \Delta t\chi/\Delta x^2 = 0.1$. Figure 18 exhibits the transient temperature fields given by GWCSTF and analytical solutions. Good agreement can be observed.

To test the accuracy of GWCSTF, its numerical errors at different mesh sizes are compared with those of TLBFS. Five different mesh sizes (80 × 80, 120 × 120, 160 × 160, 200 × 200, and 240 × 240) are considered, and other parameters are set the same as above. The numerical error quantified by the L_2 norm is defined as

$$E_2 = \sqrt{\frac{\sum_{i=1}^{N_0} (T_n - T_a)^2}{N_0}}, \tag{99}$$

where T_a and T_n are the analytical and numerical results, respectively, and N_0 is the grid amount. The numerical error is calculated at $\mathrm{Fo} = t\chi/L^2 = 0.02$.

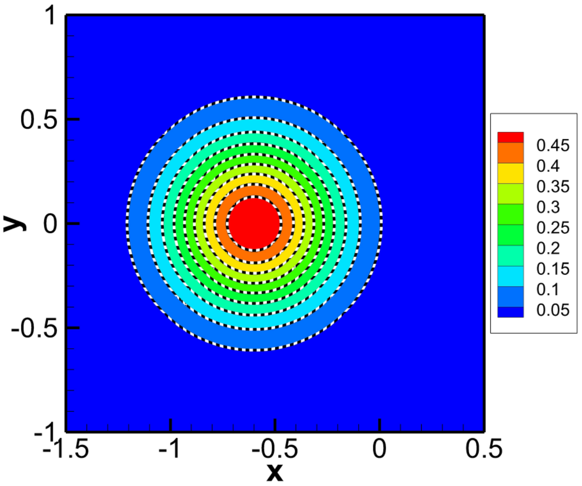

FIG. 18. Comparison of temperature contours at $\mathrm{Fo} = 0.02$ between the results given by GWCSTF (white dashed line) and analytical solution (solid black line).

Figure 19 shows that both GWCSTF and TLBFS have a convergence order near 2, which is consistent with the accuracy of the discretization scheme. Additionally, the numerical errors of GWCSIF are smaller than those of TLBFS.

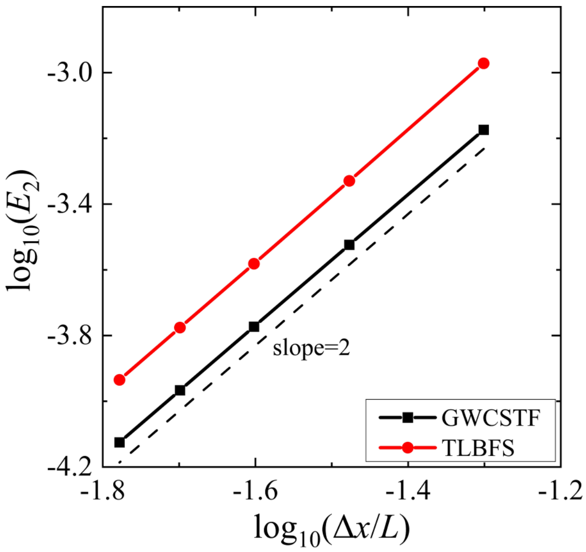

FIG. 19. Numerical errors of TLBFS and GWCSTF for convection diffusion of a Gaussian hill.

TABLE III. Comparison of characteristic parameters of natural convection at different Ra.

Ra	References	10^3	10^4	10^5	10^6
$(u_{x=0.5L}L/\chi)_{\max}$	TLBM [39]	3.644	16.134	34.261	63.024
	TLBFS [36]	3.640	16.14	34.87	64.838
	DQ [40]	3.649	16.190	34.736	64.775
	GWCSTF	3.647	16.167	34.724	64.860
y/L	TLBM [39]	0.810	0.820	0.855	0.848
	TLBFS [36]	0.815	0.825	0.855	0.850
	DQ [40]	0.815	0.825	0.855	0.850
	GWCSTF	0.8145	0.8234	0.8546	0.8501
$(v_{y=0.5L}L/\chi)_{\max}$	TLBM [39]	3.691	19.552	67.799	215.26
	TLBFS [36]	3.708	19.67	68.85	220.92
	DQ [40]	3.698	19.638	68.640	220.64
	GWCSTF	3.697	19.635	68.695	220.953
x/L	TLBM [39]	0.180	0.120	0.065	0.040
	TLBFS [36]	0.180	0.118	0.065	0.038
	DQ [40]	0.180	0.120	0.065	0.035
	GWCSTF	0.180	0.1190	0.0669	0.0379
$\mathrm{Nu_a}$	TLBM [39]	1.117	2.241	4.511	8.731
	TLBFS [36]	1.115	2.232	4.491	8.711
	DQ [40]	1.118	2.245	4.523	8.762
	GWCSTF	1.118	2.245	4.523	8.835

B. 2D natural convection in a square cavity

The 2D natural convection in a square cavity is simulated in the present subsection to validate GWCSTF for natural convection in an extensive range of Ra. The physical model is the same as that described in Sec. V B. The Prandtl number and characteristic velocity are set as $\mathrm{Pr} = 0.71$ and $V_c = 0.1$, respectively; six Rayleigh numbers (10^3, 10^4, 10^5, 10^6, 10^7, and 10^8) are chosen. According to Refs. [37,38], for $\mathrm{Ra} = 10^3$, 10^4, 10^5, and 10^6, uniform meshes are adopted, the corresponding mesh sizes are 100×100, 150×150, 200×200, and 250×250, respectively. For $\mathrm{Ra} = 10^7$ and 10^8, very fine meshes are needed in the area near walls to capture the boundary layers. Therefore, nonuniform meshes are adopted, the mesh sizes for $\mathrm{Ra} = 10^7$ and 10^8 are 300×300 and 400×400, respectively, and the distances from the wall to the nearest computational grid are $0.0004L$ and $0.0002L$, respectively.

First, the cases $\mathrm{Ra} = 10^3$, 10^4, 10^5, and 10^6 are investigated. Table III compares several characteristic parameters, including the maximum u along $x = 0.5L$ and the corresponding y coordinate, the maximum v along $y = 0.5L$ and the corresponding x coordinate, and the average Nusselt number $\mathrm{Nu_a}$ of the computational domain. $\mathrm{Nu_a}$ is defined as

$$\mathrm{Nu}_a = \frac{1}{\chi \Delta T L} \iint (uT - \chi \partial_x T) dx dy \qquad (100)$$

It can be seen that these characteristic parameters at different Ra obtained by GWCSTF agree well with the reference results [36,39,40].

Second, the test cases of high Ra (10^7 and 10^8) are investigated. Isothermals and streamlines are given in Figs. 20 and 21, respectively. At such high Ra, the velocity and temperature boundary layers near the hot and cold walls are much thinner. However, GWCSTF shows good numerical stability at such high Ra.

The u profiles along $y = 0.5L$ and v profiles along $x = 0.5L$ at $\mathrm{Ra} = 10^7$ and 10^8 obtained by GWCSIF are compared with the reference results [37,41]. As shown in Fig. 22, the present results given by GWCSIF are in good accordance with the reference results [37,41].

Furthermore, Tables IV and V provide detailed comparisons of several characteristic parameters, which include the maximum dimensionless stream function and the corresponding position, the average Nusselt number along $x = 0.5L$, the maximum u along $x = 0.5L$ and the corresponding location, and the maximum v along $y = 0.5L$ and the corresponding location, at $\mathrm{Ra} = 10^7$ and 10^8, respectively. It can be seen that the present results given by GWCSIF compare well with the results of Contrino *et al.* [42] using the multiple-relaxation-times thermal lattice Boltzmann equation, Quéré [43] applying the high-order pseudospectral method, Yang

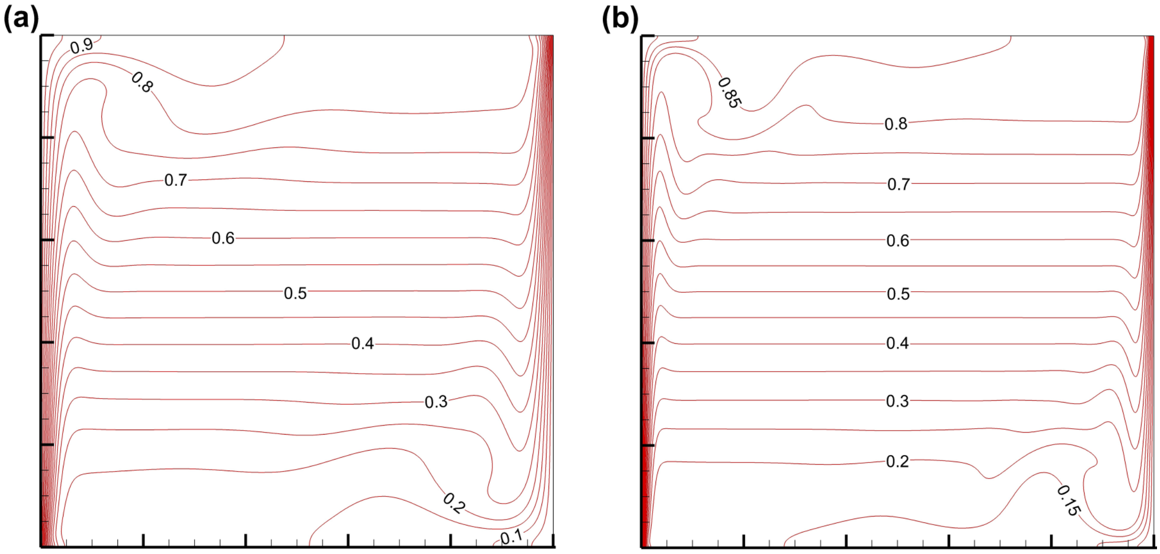

FIG. 20. Isotherms for natural convection in a square cavity at (a) $\mathrm{Ra} = 10^7$, (b) $\mathrm{Ra} = 10^8$.

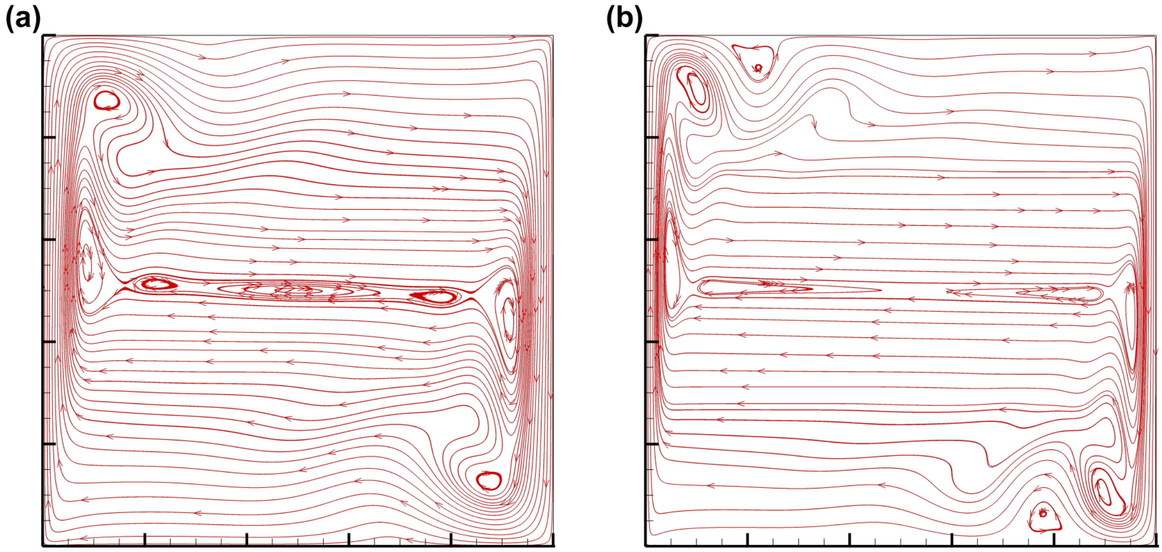

FIG. 21. Streamlines for natural convection in a square cavity at (a) $\mathrm{Ra} = 10^7$, (b) $\mathrm{Ra} = 10^8$.

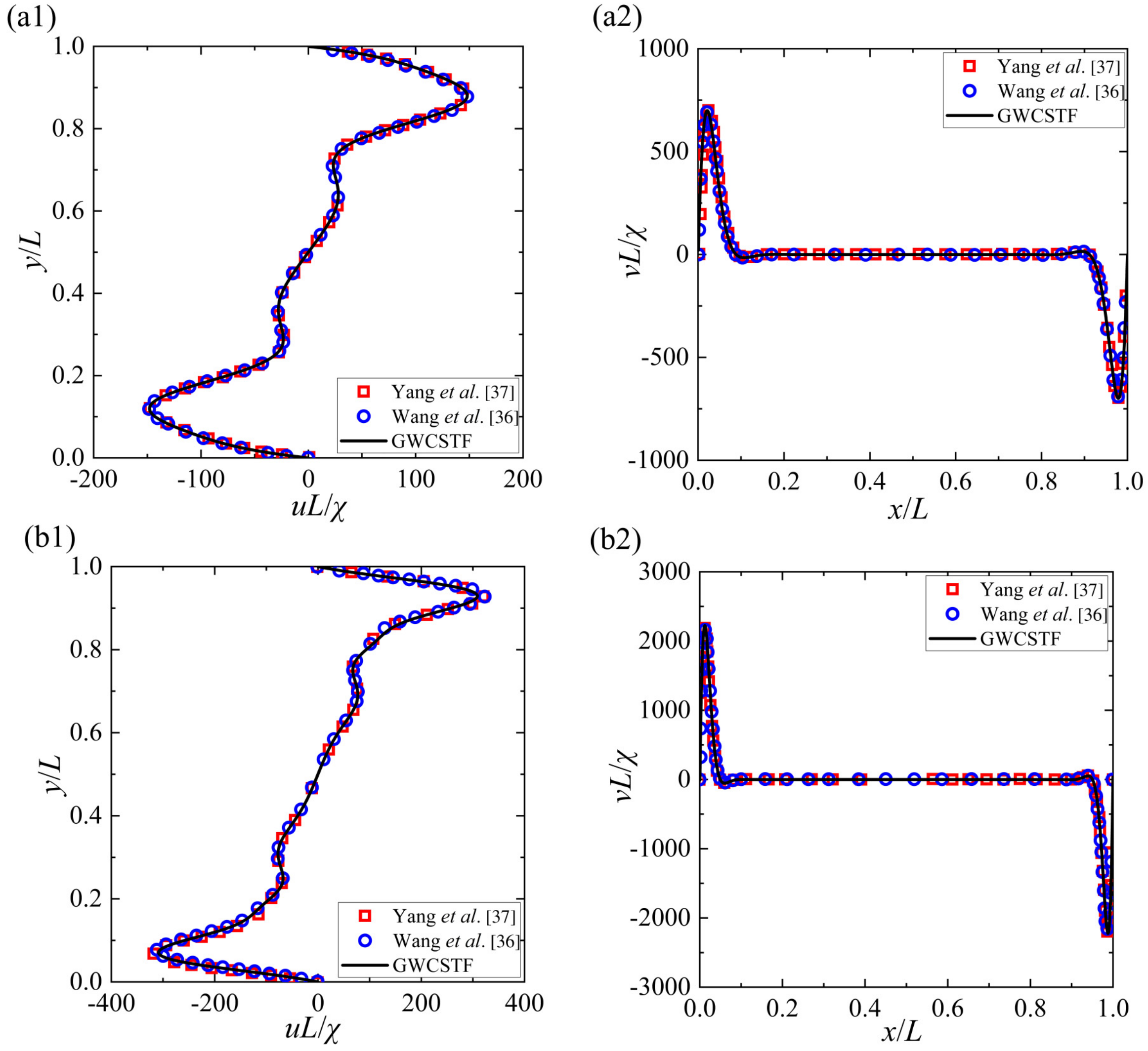

FIG. 22. The u profiles along $x = 0.5L$ and v profiles along $y = 0.5L$ at $\mathrm{Ra} = 10^7$ (a1), (a2), $\mathrm{Ra} = 10^8$ (b1), (b2), together with the data given by Yang *et al.* [37] and Wang *et al.* [36].

TABLE IV. Results of 2D natural convection in a square cavity at Ra = 10^7.

Parameters	Contrino *et al.* [42]	Quéré [43]	Wang *et al.* [36]	Yang *et al.* [37]	GWCSTF
$\vert\psi/\chi\vert_{\max}$	30.1760	30.165	30.164	30.192	30.138
x/L	0.0858	0.086	0.0857	0.0848	0.0850
y/L	0.5558	0.556	0.5559	0.5548	0.5546
$\mathrm{Nu}_{1/2}$	16.5231	16.52	16.543	16.518	16.514
$(u_{x=0.5L}L/\chi)_{\max}$	148.5852	148.59	148.84	148.86	148.05
y/L	0.8793	0.879	0.8789	0.8800	0.8801
$(v_{y=0.5L}L/\chi)_{\max}$	699.3166	699.18	699.91	699.20	699.63
x/L	0.0213	0.021	0.0216	0.0217	0.0213

et al. [37] adopting a developed gas kinetic scheme, and Wang *et al.* [36] using TLBFS.

C. 3D natural convection in a concentric annulus

To validate the flexibility of GWCSTF for 3D curved boundaries, 3D natural convection in a concentric annulus is simulated. The schematic diagram is depicted in Fig. 23. The radii of the inner and outer cylinders are R_i and R_o, respectively, and the height of the annulus is H. The geometry of the physical model is depicted by two aspect ratios, $\mathrm{Ar} = R_o/R_i$ and $\eta = H/(R_o - R_i)$.

The inner and outer cylinder surfaces have constant temperatures $T_i = 1$ and $T_o = 0$, respectively, and the top and bottom walls are adiabatic. All walls are stationary, and the nonslip boundary condition is adopted.

The problem is characterized by the Prandtl number Pr and the Rayleigh number Ra. Their definitions are

$$\mathrm{Pr} = \upsilon/\chi, \quad \mathrm{Ra} = \frac{\beta g(T_i - T_o)(R_o - R_i)^3}{\upsilon\chi} = \frac{V_c^2(R_o - R_i)^2}{\upsilon\chi}, \tag{101}$$

where V_c is the characteristic velocity defined as $V_c = \sqrt{\beta g(T_i - T_o)(R_o - R_i)}$. In the present simulation, $\mathrm{Ar} = 2$, $\eta = 2$, $\mathrm{Pr} = 0.71$, and $V_c = 0.1$ are fixed, and two Ra (10^4 and 10^5) are considered. Owing to the axisymmetric model, only one mesh layer is needed in the azimuthal direction. The mesh size used for simulations is 120 × 1 × 240.

Figures 24 and 25 show the steady streamlines at the $r-z$ plane. As the Rayleigh number increases from 10^4 to 10^5, more vortices arise in the flow field, and the thermal boundary layers become thinner. These phenomena imply enhanced heat transfer and more vigorous natural convection. These observations are consistent with those reported in Refs. [14,44].

For further validation, the average Nusselt numbers of the inner and outer cylinder surfaces obtained by GWCSTF are compared with the reference data [14,44,45]. The average Nusselt numbers of the inner and outer cylinder surfaces are defined as

$$\overline{\mathrm{Nu}}_{i,o} = -\frac{R_{i,o}}{H(T_i - T_o)} \int_0^H \left.\frac{\partial T}{\partial r}\right|_{i,o} dz, \tag{102}$$

where the subscripts i and o represent the variables of the inner and outer surfaces, respectively. As shown in Table VI, the Nusselt numbers of the inner and outer surfaces given by GWCSTF agree well with the reference data [14,44,45]. The comparison validates the ability of GWCSTF to tackle 3D curved boundaries.

VII. CONCLUSIONS

From a macroscopic perspective, directly solving weakly compressible models with the central difference schemes suffers numerical instability. Adding numerical dissipation terms is a popular approach to achieving good numerical stability. Given the general numerical dissipation terms, many weakly compressible models can be incorporated into a unified, simple framework. This idea is the motivation for the present work.

In the present paper, several weakly compressible models have been analyzed. It is found that all models contain a mass diffusion term related to $\partial_\alpha\partial_\alpha\rho$ and bulk viscosity terms related to $\partial_\alpha\partial_\beta(\rho u_\beta)$. In particular, the additional terms in FSLBM include only the mass diffusion term and the bulk viscosity term. These results indicate that the mass diffusion

TABLE V. Results of 2D natural convection in a square cavity at Ra = 10^8.

Parameters	Contrino *et al.* [42]	Quéré [43]	Wang *et al.* [36]	Yang *et al.* [37]	GWCSTF
$\vert\psi/\chi\vert_{\max}$	53.953	53.85	53.893	53.885	53.792
x/L	0.0480	0.048	0.0476	0.0476	0.0489
y/L	0.5533	0.553	0.5528	0.5532	0.5478
$\mathrm{Nu}_{1/2}$	30.227	30.225	30.301	30.227	30.191
$(u_{x=0.5L}L/\chi)_{\max}$	321.37	321.9	323.65	321.49	308.7
y/L	0.9276	0.928	0.9288	0.9284	0.9290
$(v_{y=0.5L}L/\chi)_{\max}$	2222.3	2222	2222.9	2221.7	2223.4
x/L	0.0120	0.012	0.0119	0.0122	0.0119

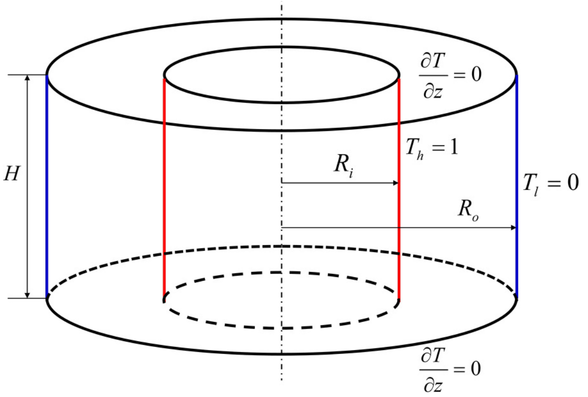

FIG. 23. Schematic diagram of the 3D natural convection in a concentric annulus.

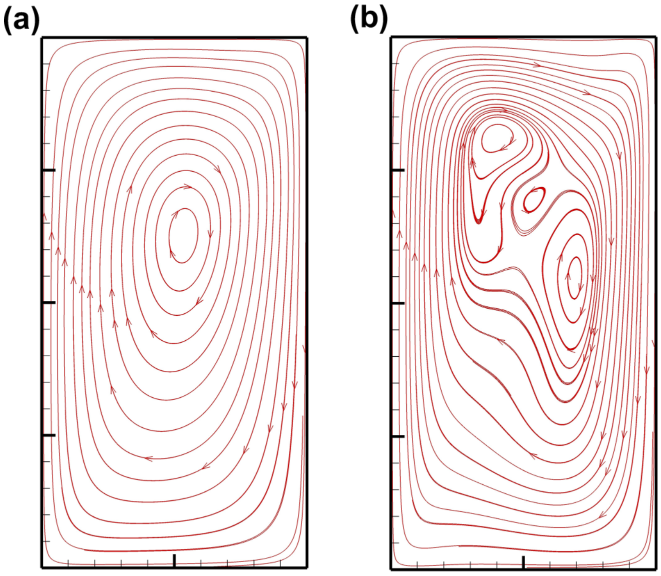

FIG. 24. Streamlines on the *r*-*z* plane of the 3D natural convection in a concentric annulus at different Ra. (a) Ra $= 10^4$, (b) Ra $= 10^5$.

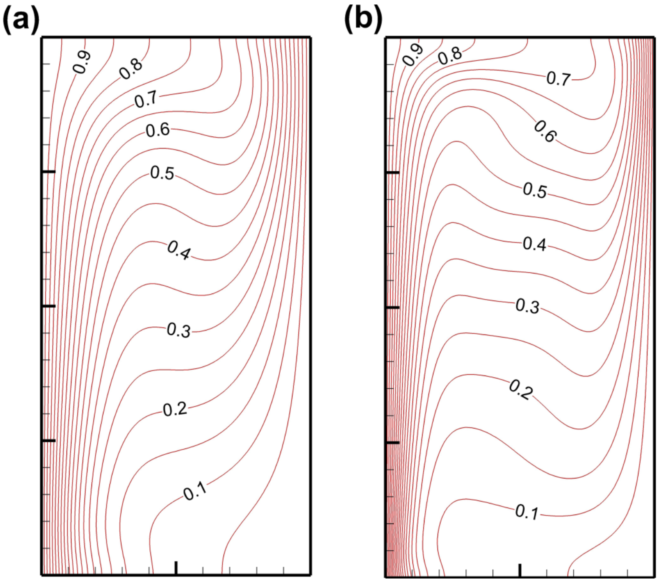

FIG. 25. Isotherms on the *r*-*z* plane of the 3D natural convection in a concentric annulus at different Ra. (a) Ra $= 10^4$, (b) Ra $= 10^5$.

and the bulk viscosity terms provide general mechanisms for stabilizing the computation of weakly compressible models.

Based on the general mechanisms and referring to computational procedures of LBFS, a general approach, which introduces numerical dissipation terms implicitly, has been proposed to construct general weakly compressible solvers using governing equations. GWCSIF was proposed first. Numerical investigations for GWCSIF and other weakly compressible models demonstrate that the general mechanisms can ensure good numerical stability for high Reynolds number flows. The general mechanisms can explain the good numerical stability of those weakly compressible models, except for LBM. LBM has intrinsic mechanisms beyond the general ones to achieve good numerical stability at large kinematic viscosities. However, its numerical stability at small kinematic viscosities is worse than the dissipative model with the general mechanisms. More numerical simulations prove that GWCSIF has similar numerical accuracy as LBFS and can simulate both viscous and inviscid, transient and steady, and 2D and 3D incompressible flows, which validates the general mechanisms further.

To show the generality of the approach of constructing general weakly compressible solvers, GWCSTF has been proposed to simulate incompressible thermal flows. Numerical investigations also show that GWCSTF has good numerical stability for high Rayleigh number flows and good accuracy. In summary, the good performances of GWCSIF and

TABLE VI. Comparison of average Nusselt numbers for the 3D natural convection in a concentric annulus.

	Reference [44]		Reference [14]		Reference [45]		Present	
Ra	$\overline{\mathrm{Nu}}_i$	$\overline{\mathrm{Nu}}_o$	$\overline{\mathrm{Nu}}_i$	$\overline{\mathrm{Nu}}_o$	$\overline{\mathrm{Nu}}_i$	$\overline{\mathrm{Nu}}_o$	$\overline{\mathrm{Nu}}_i$	$\overline{\mathrm{Nu}}_o$
10^4	3.220	3.217	3.228	3.193	3.126	3.216	3.212	3.222
10^5	5.815	5.808	5.731	5.712	5.798	5.798	5.789	5.809

GWCSTF validate the general mechanisms for stabilizing computation and the general approach to constructing general weakly compressible solvers.

ACKNOWLEDGMENT

J.L. acknowledges the support of the Alexander von Humboldt Foundation, Germany.

[1] S. V. Patankar and D. B. Spalding, Int. J. Heat Mass Transfer **15**, 1787 (1972).

[2] S. V. Patankar, Numer. Heat. Transfer **4**, 409 (1981).

[3] J. P. Van Doormaal and G. D. Raithby, Numer. Heat. Transfer **7**, 147 (1984).

[4] R. I. Issa, J. Comput. Phys. **62**, 40 (1986).

[5] A. J. Chorin, J. Comput. Phys. **2**, 12 (1967).

[6] X. He, G. D. Doolen, and T. Clark, J. Comput. Phys. **179**, 439 (2002).

[7] T. Ohwada, P. Asinari, and D. Yabusaki, Comput. Math. Appl. **61**, 3461 (2011).

[8] T. Ohwada and P. Asinari, J. Comput. Phys. **229**, 1698 (2010).

[9] P. Asinari, T. Ohwada, E. Chiavazzo, and A. F. Di Rienzo, J. Comput. Phys. **231**, 5109 (2012).

[10] Y. H. Qian, D. D'Humières, and P. Lallemand, Europhys. Lett. **17**, 479 (1992).

[11] C. Shu, X. D. Niu, Y. T. Chew, and Q. D. Cai, Math. Comput. Simul. **72**, 201 (2006).

[12] Z. Chen, C. Shu, Y. Wang, L. M. Yang, and D. Tan, Adv. Appl. Math. Mech. **9**, 1 (2017).

[13] Z. Chen, C. Shu, and D. Tan, Appl. Sci. **7**, 277 (2017).

[14] Z. Chen, C. Shu, and D. Tan, Phys. Fluids **29**, 053601 (2017).

[15] Z. Chen, C. Shu, D. Tan, and C. Wu, Int. J. Numer. Methods Fluids **87**, 161 (2018).

[16] C. Shu, Y. Wang, C. J. Teo, and J. Wu, Adv. Appl. Math. Mech. **6**, 436 (2014).

[17] Y. Wang, C. Shu, and C. J. Teo, Int. J. Numer. Methods Fluids **75**, 344 (2014).

[18] J. Lu, H. Lei, C. Shu, and C. Dai, J. Comput. Phys. **415**, 109546 (2020).

[19] J. Lu, C. Dai, and P. Yu, Phys. Fluids **33**, 107120 (2021).

[20] J. Lu, C. Dai, and P. Yu, Int. J. Heat Mass Transfer **187**, 122576 (2022).

[21] J. J. Huang, Phys. Rev. E **103**, 053311 (2021).

[22] X. He and L. S. Luo, J. Stat. Phys. **88**, 927 (1997).

[23] A. Matyas, Comput. Fluids **187**, 60 (2019).

[24] J. Lu, H. Lei, C. Dai, L. Yang, and C. Shu, J. Comput. Phys. **453**, 110923 (2022).

[25] G. Zhao-Li, Z. Chu-Guang, and S. Bao-Chang Chinese Phys. **11**, 366 (2002).

[26] X. He and G. Doolen, J. Comput. Phys. **134**, 306 (1997).

[27] L. M. Yang, C. Shu, W. M. Yang, and Y. Wang, Int. J. Numer. Methods Fluids **85**, 583 (2017).

[28] S. C. R. Dennis and G.-Z. Chang, J. Fluid Mech. **42**, 471 (1970).

[29] F. Nieuwstadt and H. B. Keller, Comput. Fluids **1**, 59 (1973).

[30] M. Braza, P. Chassaing, and H. H. Minh, J. Fluid Mech. **165**, 79 (1986).

[31] C. Liu, X. Zheng, and C. H. Sung, J. Comput. Phys. **139**, 35 (1998).

[32] H. Ding, C. Shu, and Q. D. Cai, Comput. Fluids **36**, 786 (2007).

[33] Y. Wang, C. Shu, C. J. Teo, J. Wu, and L. Yang, Commun. Comput. Phys. **18**, 593 (2015).

[34] H. Ding, C. Shu, K. S. Yeo, and D. Xu, Comput. Methods Appl. Mech. Eng. **195**, 516 (2006).

[35] Z. Chen, C. Shu, and D. Tan, Int. J. Heat Mass Transfer **105**, 741 (2017).

[36] Y. Wang, C. Shu, and C. J. Teo, Comput. Fluids **94**, 98 (2014).

[37] L. M. Yang, C. Shu, W. M. Yang, and J. Wu, Phys. Rev. E **97**, 013305 (2018).

[38] S. K. Kang and Y. A. Hassan, Comput. Fluids **49**, 36 (2011).

[39] Y. Peng, C. Shu, and Y. T. Chew, Phys. Rev. E **68**, 026701 (2003).

[40] C. Shu and H. Xue, Int. J. Heat Fluid Flow **19**, 59 (1998).

[41] Y. Wang, L. Yang, and C. Shu, Entropy **17**, 7713 (2015).

[42] D. Contrino, P. Lallemand, P. Asinari, and L. S. Luo, J. Comput. Phys. **275**, 257 (2014).

[43] P. Quéré, Comput. Fluids **20**, 29 (1991).

[44] Y. Wang, C. Shu, C. J. Teo, and L. M. Yang, Numer. Heat Transfer, Part B **69**, 111 (2016).

[45] L. Li, R. Mei, and J. F. Klausner, Int. J. Heat Mass Transfer **67**, 338 (2013).